UNIVERSITY OF CALIFORNIA,
IRVINE

Towards Opportunistic Navigation with LEO Satellites: Adaptive Clock Estimation and Closed-Loop Ephemeris Tracking

THESIS

submitted in partial satisfaction of the requirements
for the degree of

MASTER OF SCIENCE

in Mechanical and Aerospace Engineering

by

Nadim Khairallah

Thesis Committee:
Professor Zaher (Zak) M. Kassas, Chair
Professor Solmaz S. Kia
Professor Tryphon T. Georgiou

2022

DEDICATION

To my parents, Rania and Fadi, and my sister Nour.

TABLE OF CONTENTS

LIST OF FIGURES

LIST OF TABLES

ACKNOWLEDGMENTS

I would like to thank my advisor, Prof. Zak Kassas, for his support, guidance, and for everything he taught me, both technical and non-technical. I would also like to thank him for welcoming me to the ASPIN Lab and providing me with many opportunities to work on exciting projects and present my research at conferences. Finally, I would like to thank Prof. Kassas for believing in me and nominating me for the U.S. Department of Transportation Graduate Student of the Year award.

I would like to thank my committee members Prof. Solmaz Kia and Prof. Tryphon Georgiou for taking time to serve on my committee. I would also like to thank them for the courses I took with them and the lessons they taught me.

I would like to thank the Office of Naval Research (ONR), the Air Force Office of Scientific Research (AFOSR), the National Science Foundation (NSF), and the U.S. Department of Transportation (DOT) for supporting my research.

I would like to thank Joe Khalife who was a big brother and a mentor during my first year at ASPIN. Without his advice and insights, I would not be where I am today and have accomplished so much during my time at ASPIN.

I would like to thank all my labmates: Joe, Mohamad, Mu, Alex, Jamil, Ralph, Sharbel, Ali, and Mohammad. In addition to being amazing friends, they contributed to a supporting lab environment and were great colleagues to work with. I enjoyed all the activities we did together and all the discussions I had with each and everyone of them, whether related to research or not. I would also like to thank them for their help with experiments.

I would like to thank my parents, Rania and Fadi, and my sister Nour for their unconditional love and unwavering support. I would not have gotten this far without them, and I love them.

Lastly, I would like to thank all the persons I encountered in my life who had an impact on me and shaped me into the person I am today.

ABSTRACT OF THE THESIS

Towards Opportunistic Navigation with LEO Satellites:
Adaptive Clock Estimation and Closed-Loop Ephemeris Tracking

By

Nadim Khairallah

Master of Science in Mechanical and Aerospace Engineering

University of California, Irvine, 2022

Professor Zaher (Zak) M. Kassas, Chair

Low Earth orbit (LEO) satellites inherently possess desirable attributes for navigation: (i) abundance, (ii) geometric and spectral diversity, and (iii) high received powers. However, the first prerequisite to satellite navigation is to know the satellites' ephemeris (i.e., position and velocity over time) and clock error states. Unlike global navigation satellite systems (GNSS), specifically designed for navigation, with satellites in medium Earth orbit (MEO) that constantly transmit ephemeris and clock corrections to users in their signals, LEO satellites, mainly operated by private companies, generally do not openly send such information in their proprietary signals. The quality of oscillators on-board LEO satellites' as well as their clock error states are completely unknown. Moreover, the most accurate publicly available information on LEO satellites' ephemerides is in the form of two-line element (TLE) files, which yield ephemerides with errors of a few kilometers in position and a few meters per second in velocity. Consequently, LEO satellites' states are completely unknown (clock errors) or uncertain at best (ephemeris).

This thesis addresses the aforementioned challenges by performing the opportunistic estimation of LEO satellites' states. An adaptive estimator is developed to estimate in real-time the clock quality on-board LEO satellites and a complete framework is discussed to oppor-

tunistically refine the TLE-generated LEO satellites' ephemeris. The findings of this thesis are demonstrated experimentally with Orbcomm LEO satellites and are shown to improve opportunistic receiver positioning with LEO satellites' signals.

Chapter 1

Introduction

With the ongoing technological advancements, the shift to increasing autonomy is already on the horizon with the development of autonomous vehicles (AVs), urban air mobility (UAM), intelligent transportation systems, drone delivery services, etc. [1, 2]. Accurate and resilient position, navigation, and timing (PNT) is needed to guarantee a safe transition into this increasingly autonomous world and the operation of these safety-critical systems [3].

For decades, global navigation satellite systems (GNSSs) have been the universal technology for PNT services. GNSS signals, however, could become unavailable [4] (e.g., in deep urban canyons, under dense foliage, during unintentional interference, and intentional jamming) or untrustworthy (e.g., under malicious spoofing attacks) [5]. As a result, complements and/or alternatives to GNSSs have to be developed to guarantee the stringent PNT requirements of the current and future autonomous technologies [6, 7, 8, 9, 10, 11, 12, 13, 14, 15, 16, 17, 18].

Opportunistic navigation has gained significant attention in recent years to overcome the above-mentioned limitations of GNSSs [19]. This paradigm aims to exploit ambient signals of opportunity (SOPs) in the environment [20, 21, 22]. Terrestrial SOPs include AM/FM radio [23, 24], digital television [25, 26], and cellular signals [27, 28]. Of particular note,

the various generations of cellular signals (3G code-division multiple-access (CDMA), 4G long-term evolution (LTE), and 5G [29, 30, 31, 32, 33, 34, 35, 36, 37, 38, 39] have shown the potential of meter-level level accuracy on ground and aerial vehicles [40, 41, 42, 43, 44, 45, 46, 47, 48, 49, 50, 51].

As for space-based SOPs, low Earth orbit (LEO) space vehicles (SVs) have monopolized the scene recently, as they could revolutionize satellite-based navigation [52, 53, 54, 55, 56, 57, 58, 59, 60, 61, 62, 63]. LEO SVs' inherent characteristics make them desirable for navigation [64, 65]. First, LEO SVs are abundant, with around 4,000 active SVs in LEO as of January 2022 [66]. This number of LEO SVs is projected to increase dramatically over this decade due to the launch of so-called megaconstellations (e.g., Starlink, Kuiper, etc.) [67]. Fig. 1.1 shows some of the existing and future LEO megaconstellations that will form a virtual blanket cover around Earth. Second, LEO SVs' configuration relative to a receiver anywhere on Earth yields a low geometric dilution of precision (GDOP), which improves navigation accuracy [68]. Third, LEO SVs transmit in a wide range of frequency bands as seen from Table 1.1, which reduces vulnerability to interference. Fourth, LEO SVs are around twenty times closer to Earth than GNSS SVs, which reside in medium Earth orbit (MEO), making the received power of LEO signals up to 30 dB higher than their GNSS counterparts [69].

Table 1.1: Some existing and future LEO satellite constellations

	System	**Number of satellites**	**Frequency band**
Existing	Orbcomm	36	VHF
	Globalstar	48	S and C
	Iridium NEXT	66	L and Ka
Future	Boeing	147	V and Ka
	SpaceMobile	243	Ka and V
	OneWeb	882	Ku and Ka
	Telesat	1,671	Ku and Ka
	Kuiper (Amazon)	3,236	Ku and Ka
	Starlink (SpaceX)	11,943	Ku, Ka, and V

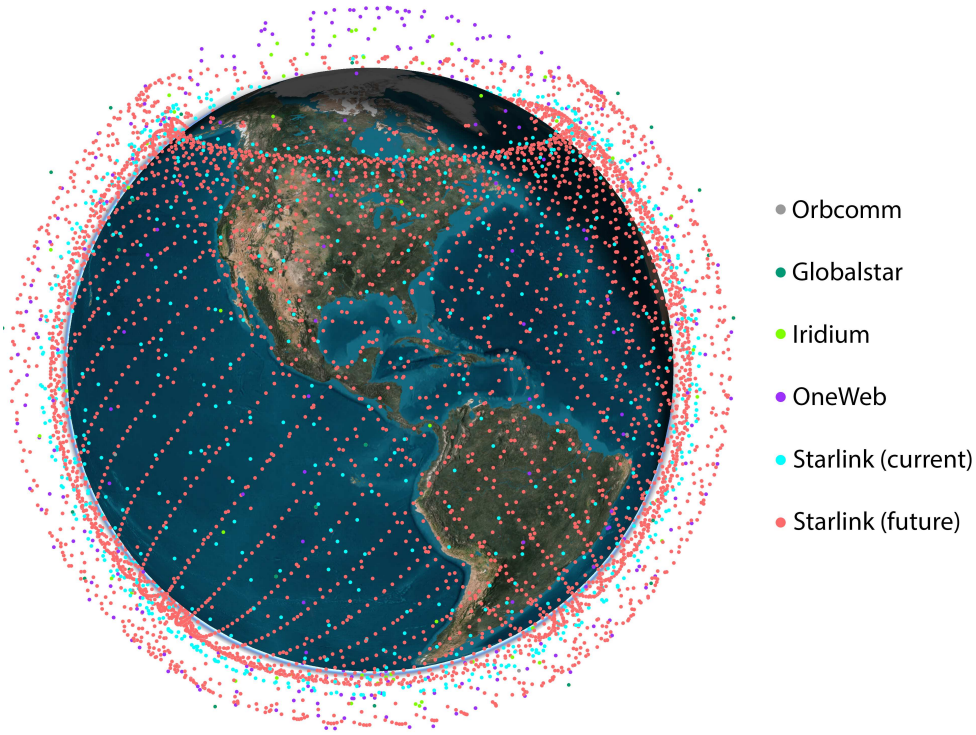

Figure 1.1: Existing and future LEO satellite constellations.

However, there are two main challenges to opportunistic navigation using LEO SVs. First, the proprietary signals transmitted by LEO SVs are partially known. This issue can be tackled with the design of specialized receivers that leverage the periodic signals with favorable correlation properties transmitted by the LEO SVs [70, 71, 72, 73, 74, 75]. Even when LEO signals are unknown, cognitive signal processing approaches [76] have been shown to yield useful navigation observables [77, 78, 79, 80, 81, 82]. Second, unlike GNSS SVs, LEO SVs generally do not openly transmit information about their clock error states and ephemeris in their downlink signals. To tackle this challenge, the simultaneous tracking and navigation (STAN) framework was proposed, in which the receiver estimates its own states simultaneously with the states of the LEO SVs [83, 84].

More specifically, the lack of timing and ephemeris information openly transmitted in LEO SVs' downlink signals manifests itself with the following practical challenges. On one hand, the quality of oscillators on-board LEO SVs is generally unknown and no information is

available on the degree of synchronicity of clocks across the constellation network. On the other hand, among the most accurate publicly available information on ephemerides are two-line element (TLE) files, published and updated periodically by the North American Aerospace Defense Command (NORAD) [85]. These TLE files consist of a set of mean Keplerian elements (inclination angle, right ascension of ascending node, eccentricity, argument of perigee, mean anomaly, and mean motion) and corrective terms given at a specified epoch that an analytical Simplified General Perturbation (SGP4) model [86] can propagate to any inquiry time. Although SGP4 takes into account the variation of the orbital elements due to Earth's oblateness, atmospheric drag, and various short and long-term perturbations, the TLE-propagated SV ephemerides suffer from errors of a few kilometers in position and a few meters per second in velocity compared to the actual SV ephemerides. The magnitude of the LEO SV position error as calculated from the SGP4-propagated TLE ephemeris can range from a few hundred meters to a few kilometers, but with the most error concentrated in the along-track axis of the LEO SV's body frame.

Beyond low-fidelity analytical propagators such as SGP4 that improve computational efficiency at the cost of orbit determination accuracy, high-fidelity numerical propagators that perform costly numerical integration with complex force models can achieve higher propagation accuracies [87]. One such example of numerical propagator is Analytical Graphics Inc.'s Systems Tool Kit (STK) [88] high-precision orbit propagator (HPOP) [89]. Moreover, semi-analytical models such as Draper semi-analytical satellite theory (DSST) offer trade-offs between the accuracy of numerical propagators and the computational efficiency of analytical propagators [90]. However, all numerical and semi-analytical propagators require sufficient prior knowledge of various force model parameters (e.g., atmospheric drag, solar radiation pressure, etc.) as well as an accurate initial estimate [91, 92], which are not readily available. Additionally, erroneous model parameters or initial estimates will cause these propagators to diverge due to model mismatches.

The current state-of-the-art orbit determination technologies rely on an array of large telescopes, electro-optical surveillance systems, and radars scattered around the globe as part of the Space Surveillance Network (SSN). Operated by the Combined Space Operations Center (CSpOC), the SSN keeps track of more than 23,000 objects in orbit for space situational awareness (SSA) purposes [93] using range, angle, and optical measurements from the radars, telescopes, and electro-optical surveillance systems. These observations are used to periodically update the TLE files published online. Furthermore, machine learning was explored to tackle the orbit determination problem and reduce ephemeris errors in [94, 95, 96, 97, 98, 99, 100, 101, 102]. Although showing great promise, these machine learning approaches lack formal guarantees of performance.

To summarize the aforementioned challenges, LEO SVs' states are completely unknown (clock errors) or uncertain at best (ephemeris). The contributions of this thesis are twofold and comprehensively address the unknown LEO SVs' states challenge with the goal of enabling LEO-based opportunistic navigation.

First, the challenge of the unknown clock quality on-board LEO SVs resulting in an unknown process noise covariance for the clock error states is tackled:

- An interacting multiple model (IMM) estimator is developed to adaptively estimate the oscillator stability on-board LEO SVs in real-time while opportunistically localizing a receiver.
- The IMM estimator is implemented experimentally to characterize Orbcomm SVs' clock quality and the efficacy of the IMM adaptation is demonstrated in the context of receiver localization.

Second, a complete framework to perform the opportunistic tracking of LEO SVs by a receiver opportunistically extracting navigation observables from their downlink signals is developed:

- A methodology to compute the LEO SVs' orbital motion process noise covariance is proposed.
- LEO SV's ephemeris refinement via opportunistic tracking is performed in extensive Monte Carlo simulations with three different set of measurements: (i) pseudorange measurements, (ii) Doppler measurements, and (iii) fused pseudorange and Doppler measurements.
- The experimental tracking of an Orbcomm LEO SV using carrier phase observables opportunistically extracted from its downlink signal is performed and the ephemeris refinement performance is verified with respect to the ground truth ephemeris.
- The efficacy of the Orbcomm SV tracking is validated in the context of receiver localization and demonstrates the potential of this framework to enable LEO-based opportunistic navigation.

This thesis is organized as follows. Chapter 2 presents the LEO SV's orbital dynamics, the measurement models, and the ionospheric and tropospheric models used to correct for atmospheric effects. Chapter 3 tackles the adaptive real-time estimation of the LEO SV's on-board oscillator quality for improved receiver positioning. Chapter 4 presents a comprehensive framework to perform the tracking of LEO SVs by a receiver opportunistically extracting navigation observables from the LEO SVs' signals. The contributions of this thesis are summarized in Chapter 5.

The intellectual products from this thesis are published in the following journal and conference articles.

Journal Publication

[J1] N. Khairallah and Z. Kassas (2022) "Ephemeris tracking and error propagation analysis of LEO satellites for opportunistic navigation," *IEEE Transactions on Aerospace and Electronic Systems*, in preparation.

Conference Publications

[C1] N. Khairallah and Z. Kassas (2021) "Ephemeris closed-loop tracking of LEO satellites with pseudorange and Doppler measurements," *in Proceedings of ION GNSS Conference*, Sep. 20–24, St. Louis, MO, pp. 2544–2555.

[C2] N. Khairallah and Z. Kassas (2022) "An interacting multiple model estimator of LEO satellite clocks for improved positioning," *in Proceedings of IEEE Vehicular Technology Conference*, Jun. 13–22, Helsinki, Finland, accepted.

Chapter 2

Model Description

This chapter presents the LEO satellites' orbital dynamics; the pseudorange, Doppler, pseudorange rate, and carrier phase measurement models; and the ionospheric and tropospheric models used to correct for the atmospheric effect on the measurements.

2.1 LEO Satellite Orbital Dynamics

A two-body model including the most significant non-zero mean perturbing acceleration is adopted as the LEO satellite orbital dynamics model in the Earth-centered inertial (ECI) reference frame. This model offers a trade-off between accurate open-loop state prediction while maintaining a simple analytical Jacobian for estimation error covariance propagation. The most significant perturbing accelerations for a LEO satellite are due to Earth's non-uniform gravity $\boldsymbol{a}_{\text{grav}}$. The two-body model can be written generally as

$$\ddot{\boldsymbol{r}}_{\text{leo}} = \boldsymbol{a}_{\text{grav}} + \tilde{\boldsymbol{w}}_{\text{leo}}, \qquad \boldsymbol{a}_{\text{grav}} = \frac{\partial U}{\partial \boldsymbol{r}_{\text{leo}}}, \tag{2.1}$$

where $\boldsymbol{r}_{\text{leo}} \triangleq [x_{\text{leo}},\, y_{\text{leo}},\, z_{\text{leo}}]^{\mathsf{T}}$ is the position vector of the LEO satellite in the ECI frame, U is the non-uniform gravitational potential of Earth at the satellite, and $\tilde{\boldsymbol{w}}_{\text{leo}}$ is a process noise vector in the ECI frame with power spectral density (PSD) $\tilde{\mathbf{Q}}_{\text{leo}}$, which attempts to capture the overall acceleration perturbations including the unmodeled non-uniformity of Earth's gravitational field, atmospheric drag, solar radiation pressure, third-body gravitational forces (e.g., gravity of the Moon and Sun), and general relativity [103].

Several models have been developed for Earth's gravitational potential U. For a satellite requiring accuracies of a few meters, the JGM-3 model developed by Goddard Space Flight Center is usually sufficient [104]. Here, the tesseral and sectoral terms of the JGM-3 model are neglected, since they are several orders of magnitude smaller than the zonal terms (denoted $\{J_n\}_{n=2}^{\infty}$). This yields [105]

$$U = \frac{\mu}{\|\boldsymbol{r}_{\text{leo}}\|}\left[1 - \sum_{n=2}^{N} J_n \frac{R_e^n}{\|\boldsymbol{r}_{\text{leo}}\|^n} P_n\left[\sin(\varphi)\right]\right], \tag{2.2}$$

where μ is Earth's standard gravitational parameter, P_n is a Legendre polynomial with harmonic n, J_n is the n-th zonal coefficient, R_e is the mean radius of the Earth, $\sin(\varphi) = z_{\text{leo}}/\|\boldsymbol{r}_{\text{leo}}\|$ (i.e., φ being the LEO SV's latitude), and $N = \infty$. Since the acceleration due to the J_2 coefficient is approximately three orders of magnitude greater than the acceleration due to the other zonal coefficients modeling Earth's oblateness, the perturbation due to non-uniform gravity will be approximated by using only the term corresponding to J_2. Taking the partial derivative of (2.2) with respect to the components of $\boldsymbol{r}_{\text{leo}}$ with $N \equiv 2$ gives the

components of $\boldsymbol{a}_{\text{grav}} \triangleq [\ddot{x}_{\text{grav}},\, \ddot{y}_{\text{grav}},\, \ddot{z}_{\text{grav}}]^{\mathsf{T}}$ in the ECI frame as [106]

$$\begin{aligned}
\ddot{x}_{\text{grav}} &= -\frac{\mu x_{\text{leo}}}{\|\boldsymbol{r}_{\text{leo}}\|^3}\left[1 + J_2\frac{3}{2}\left(\frac{R_e}{\|\boldsymbol{r}_{\text{leo}}\|}\right)^2\left(1 - 5\frac{z_{\text{leo}}^2}{\|\boldsymbol{r}_{\text{leo}}\|^2}\right)\right], \\
\ddot{y}_{\text{grav}} &= -\frac{\mu y_{\text{leo}}}{\|\boldsymbol{r}_{\text{leo}}\|^3}\left[1 + J_2\frac{3}{2}\left(\frac{R_e}{\|\boldsymbol{r}_{\text{leo}}\|}\right)^2\left(1 - 5\frac{z_{\text{leo}}^2}{\|\boldsymbol{r}_{\text{leo}}\|^2}\right)\right], \\
\ddot{z}_{\text{grav}} &= -\frac{\mu z_{\text{leo}}}{\|\boldsymbol{r}_{\text{leo}}\|^3}\left[1 + J_2\frac{3}{2}\left(\frac{R_e}{\|\boldsymbol{r}_{\text{leo}}\|}\right)^2\left(3 - 5\frac{z_{\text{leo}}^2}{\|\boldsymbol{r}_{\text{leo}}\|^2}\right)\right].
\end{aligned} \tag{2.3}$$

2.2 Clock Error Dynamics

The receiver and LEO SV clock error states are modeled according to the standard double integrator model with bias δt and drift $\dot{\delta} t$ [107]. The clock drift evolves as a random walk (i.e., the drift rate is a white noise process) and the bias is obtained by integrating the drift corrupted by additional white process noise as shown in the block diagram of Fig. 2.1.

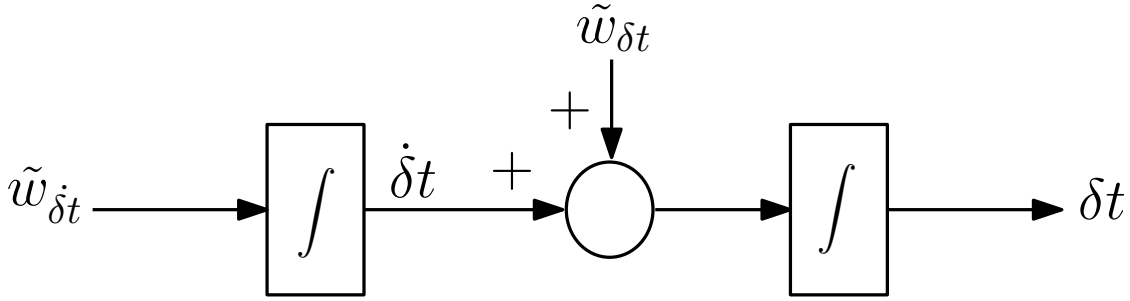

Figure 2.1: Clock error states double integrator model.

The clock error states evolve in continuous-time according to

$$\dot{\boldsymbol{x}}_{\text{clk}}(t) = \mathbf{A}_{\text{clk}}\, \boldsymbol{x}_{\text{clk}}(t) + \tilde{\boldsymbol{w}}_{\text{clk}}(t), \tag{2.4}$$

$$\boldsymbol{x}_{\text{clk}} = \begin{bmatrix} \delta t \\ \dot{\delta} t \end{bmatrix}, \quad \tilde{\boldsymbol{w}}_{\text{clk}} = \begin{bmatrix} \tilde{w}_{\delta t} \\ \tilde{w}_{\dot{\delta} t} \end{bmatrix}, \quad \mathbf{A}_{\text{clk}} = \begin{bmatrix} 0 & 1 \\ 0 & 0 \end{bmatrix},$$

where $\tilde{w}_{\delta t}$ and $\tilde{w}_{\dot{\delta} t}$ are zero-mean, mutually independent white noise processes with power

spectral density $S_{\tilde{w}_{\delta t}}$ and $S_{\tilde{w}_{\dot{\delta} t}}$, respectively. These power spectra $S_{\tilde{w}_{\delta t}}$ and $S_{\tilde{w}_{\dot{\delta} t}}$ can be related to the power-law coefficients $\{h_\alpha\}_{\alpha=-2}^{2}$, which have been shown through laboratory experiments to be adequate to characterize the power spectral density of the fractional frequency deviation $y(t)$ of an oscillator from nominal frequency, which takes the form $S_y(f) = \sum_{\alpha=-2}^{2} h_\alpha f^\alpha$ [108]. It is common to approximate the clock error dynamics by considering only the frequency random walk coefficient h_{-2} and the white frequency coefficient h_0, which lead to $S_{\tilde{w}_{\delta t}} \approx \frac{h_0}{2}$ and $S_{\tilde{w}_{\dot{\delta} t}} \approx 2\pi^2 h_{-2}$ [109].

Discretizing (2.4) at a constant sampling period T yields

$$\boldsymbol{x}_{\text{clk}}\left(k+1\right) = \mathbf{F}_{\text{clk}}\, \boldsymbol{x}_{\text{clk}}(k) + \boldsymbol{w}_{\text{clk}}(k), \quad k = 0, 1, 2, \ldots \tag{2.5}$$

where $\boldsymbol{w}_{\text{clk}}$ is a zero-mean white noise sequence with covariance $\mathbf{Q}_{\text{clk}}$

$$\mathbf{Q}_{\text{clk}} = \begin{bmatrix} S_{\tilde{w}_{\delta t}} T + S_{\tilde{w}_{\dot{\delta} t}} \frac{T^3}{3} & S_{\tilde{w}_{\dot{\delta} t}} \frac{T^2}{2} \\ S_{\tilde{w}_{\dot{\delta} t}} \frac{T^2}{2} & S_{\tilde{w}_{\dot{\delta} t}} T \end{bmatrix}, \quad \mathbf{F}_{\text{clk}} = \begin{bmatrix} 1 & T \\ 0 & 1 \end{bmatrix}. \tag{2.6}$$

2.3 Pseudorange Measurement Model

A LEO receiver extracts pseudorange measurements ρ from LEO SVs by estimating the time-of-arrival. The pseudorange ρ_l from the l-th LEO SV to the receiver at time-step k, which represents discrete-time instant $t_k = kT + t_0$ for an initial time t_0, is modeled as

$$\rho_l(k) = \left\| \boldsymbol{r}_r(k) - \boldsymbol{r}_{\text{leo}_l}(k_l') \right\|_2 + c\left[\delta t_r(k) - \delta t_{\text{leo}_l}(k_l')\right] + c\delta t_{\text{iono}_l}(k) + c\delta t_{\text{tropo}_l}(k) + v_{\rho_l}(k), \tag{2.7}$$

where k_l' represents discrete-time at $t_{k_l'} = kT + t_0 - \delta t_{\text{TOF}_l}$, with δt_{TOF_l} being the true time-of-flight of the signal from the l-th LEO SV to the receiver; $\boldsymbol{r}_r$ and $\boldsymbol{r}_{\text{leo}_l}$ are the receiver's and the l-th LEO SV's three-dimensional (3-D) position vectors expressed in the same reference

frame, respectively; c is the speed of light; δt_r and δt_{leo_l} are the receiver's and l-th LEO SV transmitter's clock biases, respectively; δt_{iono_l} and $\delta t_{\text{tropo}_l}$ are the ionospheric and tropospheric delays affecting the l-th LEO SV's signal, respectively; and $v_{\rho_l}(k)$ is the pseudorange measurement noise, which is modeled as a zero-mean white Gaussian random sequence with variance $\sigma^2_{\rho_l}(k)$.

2.4 Doppler Measurement Model

A LEO receiver extracts Doppler frequency measurements f_D from LEO SVs by subtracting the nominal carrier frequency from the received signal frequency. A pseudorange rate measurement $\dot{\rho}$ can be obtained from

$$\dot{\rho} = -\frac{c}{f_c} f_D, \tag{2.8}$$

where f_c is the carrier frequency.

The pseudorange rate measurement $\dot{\rho}_l$ from the l-th LEO SV to the receiver at time-step k can be parameterized as follows

$$\begin{aligned}\dot{\rho}_l(k) = \; & [\dot{\boldsymbol{r}}_r(k) - \dot{\boldsymbol{r}}_{\text{leo}_l}(k'_l)]^{\mathsf{T}} \frac{[\boldsymbol{r}_r(k) - \boldsymbol{r}_{\text{leo}_l}(k'_l)]}{\|\boldsymbol{r}_r(k) - \boldsymbol{r}_{\text{leo}_l}(k'_l)\|_2} + c\left[\dot{\delta}t_r(k) - \dot{\delta}t_{\text{leo}_l}(k'_l)\right] + \\ & c\dot{\delta}t_{\text{iono}_l}(k) + c\dot{\delta}t_{\text{tropo}_l}(k) + v_{\dot{\rho}_l}(k),\end{aligned} \tag{2.9}$$

where $\dot{\boldsymbol{r}}_r$ and $\dot{\boldsymbol{r}}_{\text{leo}_l}$ are the receiver's and the l-th LEO SV's 3-D velocity vectors expressed in the same reference frame as $\boldsymbol{r}_r$ and $\boldsymbol{r}_{\text{leo}_l}$, respectively; $\dot{\delta}t_r$ and $\dot{\delta}t_{\text{leo}_l}$ are the receiver's and the l-th LEO SV's transmitter clock drifts, respectively; $\dot{\delta}t_{\text{iono}_l}$ and $\dot{\delta}t_{\text{tropo}_l}$ are the drifts of the ionospheric and tropospheric delays affecting the l-th LEO SV's signal, respectively; and $v_{\dot{\rho}_l}(k)$ is the pseudorange rate measurement noise, which is modeled as a zero-mean white

Gaussian random sequence with variance $\sigma^2_{\dot{\rho}_l}(k)$.

2.5 Carrier Phase Measurement Model

The continuous-time carrier phase observable can be obtained by integrating the Doppler measurement over time [110]. The carrier phase measurement ϕ_l (expressed in meters) made by the receiver on the l-th LEO SV at time-step k can be modeled as

$$\phi_l(k) = \|\boldsymbol{r}_r(k) - \boldsymbol{r}_{\text{leo}_l}(k'_l)\|_2 + c\left[\delta t_r(k) - \delta t_{\text{leo}_l}(k'_l)\right] + \lambda_l N_l + c\delta t_{\text{iono},l}(k) + c\delta t_{\text{tropo},l}(k) + v_{\phi_l}(k), \tag{2.10}$$

where λ_l is the wavelength of the carrier signal transmitted by the l-th LEO SV, N_l is the carrier phase ambiguity of the l-th LEO SV carrier phase measurement, and $v_{\phi_l}(k)$ is the measurement noise, which is modeled as a zero-mean white Gaussian random sequence with variance $\sigma^2_{\phi_l}(k)$.

2.6 Ionospheric and Tropospheric Correction Models

Standard models [110] are used to correct for the ionospheric and tropospheric effects on the measurement models (2.7)-(2.10). In general, ionospheric and tropospheric delays can be modeled as the product of the delay at zenith and a mapping function of the LEO SV's elevation angle θ, known as the obliquity factor [110]. As the elevation angle of the SV decreases, the obliquity factor increases due to the fact that signals at low elevation angles propagate longer in the ionosphere and troposphere.

2.6.1 Ionospheric Correction Model

The ionospheric delay at zenith $c\delta t_{\text{iono,z}}$ is typically given by

$$c\delta t_{\text{iono,z}} = \frac{40.3 \times 10^{16}\ \text{TECV}}{f_c^2} \tag{2.11}$$

where f_c is the carrier frequency in Hz, TECV is the total electron content (TEC) in the vertical direction, expressed in TEC units (TECUs). NASA's Jet Propulsion Laboratory (JPL) maintains a real-time global map of the ionosphere's TEC [111]. Additionally, archived TEC maps validated by the International GNSS Service (IGS) using dual-frequency GNSS observations are available at [112].

The ionospheric delay obliquity factor $f_{\text{iono}}(\theta)$ is computed using the thin shell model as [110]

$$f_{\text{iono}}(\theta) = \left[1 - \left(\frac{R_e \cos\theta}{R_e + h_I}\right)^2\right]^{-\frac{1}{2}}, \tag{2.12}$$

where $h_I \approx 350$ km is the mean ionospheric height.

The time-history of the ionospheric delay $c\delta t_{\text{iono}}$ is consequently given by

$$c\delta t_{\text{iono}}(k) = c\delta t_{\text{iono,z}} \cdot f_{\text{iono}}(\theta), \tag{2.13}$$

where the LEO SV's elevation angle θ varies at each time-step k.

2.6.2 Tropospheric Correction Model

The effect of the tropospheric delay on the measurements is split into wet and dry components. The tropospheric wet $c\delta t_{\text{tropo}_w,\text{z}}$ and dry $c\delta t_{\text{tropo}_d,\text{z}}$ delays at zenith are computed

using the Hopfield model [110]

$$c\delta t_{\mathrm{tropo}_w,\mathrm{z}} = 0.373\frac{e_0}{T_0^2}\frac{h_w}{5} \qquad\qquad c\delta t_{\mathrm{tropo}_d,\mathrm{z}} = 77.6\times 10^{-6}\frac{P_0}{T_0}\frac{h_d}{5}, \tag{2.14}$$

where T_0 is the temperature in Kelvin, P_0 is the total pressure and e_0 is the partial pressure of water vapor in millibars, $h_w = 12$ km, and $h_d \approx 43$ km.

The tropospheric wet $f_{\mathrm{tropo}_w}(\theta)$ and dry $f_{\mathrm{tropo}_d}(\theta)$ obliquity factors are given by

$$f_{\mathrm{tropo}_w}(\theta) = \frac{1}{\sin\theta + \frac{0.00035}{\tan\theta+0.017}} \qquad\qquad f_{\mathrm{tropo}_d}(\theta) = \frac{1}{\sin\theta + \frac{0.00143}{\tan\theta+0.0445}} \tag{2.15}$$

The time-history of the tropospheric delay $c\delta t_{\mathrm{tropo}}$ is consequently given by

$$c\delta t_{\mathrm{tropo}}(k) = c\delta t_{\mathrm{tropo}_w,\mathrm{z}}\cdot f_{\mathrm{tropo}_w}(\theta) + c\delta t_{\mathrm{tropo}_d,\mathrm{z}}\cdot f_{\mathrm{tropo}_d}(\theta), \tag{2.16}$$

where the LEO SV's elevation angle θ varies at each time-step k.

Chapter 3

Adaptive Real-Time Estimation of LEO Satellite Clock Quality

This chapter develops an interacting multiple-model (IMM) estimator to adaptively estimate the clock error states process noise covariance during the localization of a stationary receiver to improve positioning accuracy and consistency [113].

3.1 Adaptive Estimation Overview

Broadly speaking, the field of adaptive estimation considers the estimation of variables such as model parameters in addition to the states of interest. In this chapter, the process noise covariance of the clock error states is adapted and so the adaptive estimation techniques of the process noise covariance are considered. These techniques can be divided into two main categories: feedback-free and feedback methods [114]. On one hand, the feedback-free methods first perform non-optimal state estimation using an initial non-matched guess of the process noise covariance matrix before updating the estimate of the process noise

covariance matrix based on a statistical analysis of the innovation sequence. On the other hand, feedback methods are inherently adaptive algorithms with the unknown process noise covariance and states estimated jointly in real-time.

Feedback-free methods include maximum likelihood and correlation methods. The maximum likelihood methods are based on the expectation-maximization (EM) algorithm: the states are estimated given a prior process noise covariance matrix in the expectation step and then the process noise covariance is updated by maximizing its likelihood in the maximization step [115]. The correlation methods are based on statistical analysis of the innovation (i.e., measurement prediction error) sequence [116] with the estimation of the entries of the process noise covariance matrix usually framed as a least-squares (LS) problem [117].

Since the application considered in this chapter, opportunistic localization, requires real-time adaptation of the clock error states process noise covariance, only feedback methods are considered. Feedback methods include covariance matching and Bayesian multiple-model estimation. Covariance matching aims at making the process noise covariance estimates consistent with the state estimate errors [118]. However, the process noise covariance matrix estimate is not guaranteed to be positive definite [119]. Ad-hoc methods can be used to enforce positive-definiteness but with no guarantees of convergence of the process noise covariance matrix estimate to its true value [120].

Following the aforementioned shortcomings of covariance matching methods, Bayesian multiple-model (MM) estimators [121] will be investigated for the online adaptation of the clock error states process noise covariance in opportunistic localization. MM estimation has been used in a variety of applications, ranging from positioning and navigation [122, 123], target tracking [124, 125], air traffic control [126, 127], fault detection [128, 129], cognitive radio [130, 131], etc. Furthermore, MM estimators have been "adapted" to estimate process and measurement noise statistics [132].

In MM estimation, a bank of filters, traditionally Kalman filters (KFs), run in parallel, with each filter in the bank matched to a mode. The output of the MM estimator is obtained by weighing each filter's estimate by their respective innovation likelihood [109]. For systems modeled with Markovian switching probabilities between modes, the computational cost of the exhaustive MM estimator, which keeps track of all mode combinations, grows exponentially with time. Several sub-optimal filters such as the generalized pseudo-Bayesian (GPB) algorithms have been developed to remedy this issue by considering the one-step time history for GPB1 (r hypotheses) and two-step time history for GPB2 (r^2 hypotheses), where r is the number of modes [109]. The interacting multiple-model (IMM) was developed to allow for a two-step history processing using only r filters running in parallel via a mixing stage that computes the initial condition fed to each filter. As a result, the IMM, which has the computational cost of GPB1 but with comparable performance to GPB2, offers a tradeoff between complexity and adaptation capability [133], and is selected as the adaptive filter used in this chapter.

3.2 Interacting Multiple Model Estimator

A single cycle of the IMM for r modes is depicted in Fig. 3.1, with the following notational definitions:

r	Number of filters
i	$\{1, \ldots, r\} \in \mathbb{N}$
$\hat{\boldsymbol{x}}^i(k-1\|k-1)$	State estimate of filter i
$\mathbf{P}^i(k-1\|k-1)$	Estimation error covariance of filter i
$\mathbf{M}(k-1\|k-1)$	Mixing probability matrix
$\hat{\boldsymbol{x}}^{0i}(k-1\|k-1)$	Mixed initial condition matched to filter i
$\mathbf{P}^{0i}(k-1\|k-1)$	Estimation error covariance associated with $\hat{\boldsymbol{x}}^{0i}(k-1\|k-1)$
$\boldsymbol{z}(k)$	Measurement
$\Lambda_i(k)$	Innovation likelihood of filter i
$\hat{\boldsymbol{x}}^i(k\|k)$	Updated state estimate of filter i
$\mathbf{P}^i(k\|k)$	Updated estimation error covariance of filter i
$\boldsymbol{\pi}$	Mode transition probability matrix
$\boldsymbol{\mu}(k)$	Mode probability vector
$\hat{\boldsymbol{x}}(k\|k)$	Combined state estimate
$\mathbf{P}(k\|k)$	Combined estimation error covariance

The IMM algorithm consists of the four following stages, shown in Fig. 3.1, repeated recursively:

Interaction/mixing: This stage calculates the initial conditions $\hat{\boldsymbol{x}}^{0i}(k-1|k-1)$ and $\mathbf{P}^{0i}(k-1|k-1)$ fed to each filter in the bank by combining $\hat{\boldsymbol{x}}^i(k-1|k-1)$ and $\mathbf{P}^i(k-1|k-1)$ using the mixing probability matrix $\mathbf{M}(k-1|k-1)$.

Mode-matched filtering: This stages performs a regular KF update (prediction and correction), for each KF in the bank, where each filter is matched to a particular mode. It also calculates the innovation likelihood of each filter.

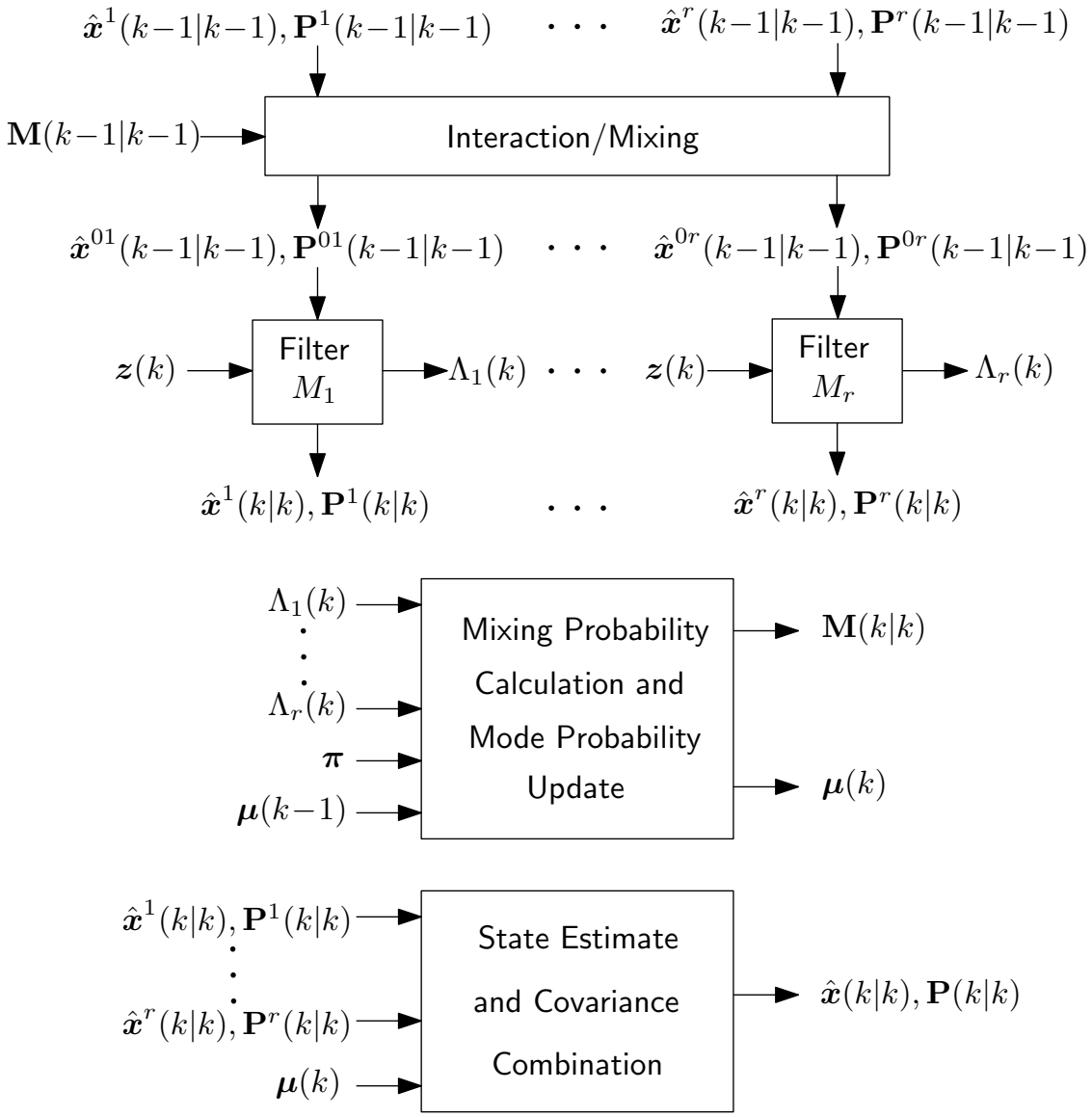

Figure 3.1: A single cycle of the IMM filter with r modes.

Mixing probability and mode probability update: This stage computes the mixing probability matrix and updates the mode probability vector, based on the innovation likelihood of each filter in the bank.

State estimate and covariance combination: This stage combines the state estimates and estimation error covariances from the individual filters by weighting $\hat{\boldsymbol{x}}^i(k|k)$ and $\mathbf{P}^i(k|k)$ by their respective mode probabilities from $\boldsymbol{\mu}(k)$.

In this chapter, an IMM adaptive filter is implemented to estimate the clock error states' process noise covariance online to improve the localization of an unknown receiver.

The process noise covariance of the clock error states depends on the corresponding oscillator stability. The quality of oscillators varies widely between temperature-compensated crystal oscillator (TCXO), oven-controlled crystal oscillator (OCXO), and chip-scale atomic clock (CSAC). The discrete-time process noise covariance for clock error states is readily calculated from (2.6), where the power spectral densities $S_{\tilde{w}_{\delta t}}$ and $S_{\tilde{w}_{\dot{\delta} t}}$ depend on the power-law coefficients associated with the oscillator stability. Table 4.1 summarizes the power-law coefficients of various clock qualities.

Table 3.1: Power-law coefficients for different oscillator qualities.

Quality	**Coefficients $\{h_0, h_{-2}\}$**
Worst TCXO	$\{2.0 \times 10^{-19}, 2.0 \times 10^{-20}\}$
Typical TCXO	$\{9.4 \times 10^{-20}, 3.8 \times 10^{-21}\}$
Typical OCXO	$\{8.0 \times 10^{-20}, 4.0 \times 10^{-23}\}$
Best OCXO	$\{2.6 \times 10^{-22}, 4.0 \times 10^{-26}\}$
CSAC	$\{7.2 \times 10^{-21}, 2.7 \times 10^{-27}\}$

Assuming no cycle slip occurs when the receiver tracks the carrier phase (i.e., the carrier phase ambiguity remains constant), the difference between the receiver and the LEO SV range-equivalent clock biases and the range-equivalent carrier phase ambiguity are lumped into a single term $c\Delta\delta t(k)$, simplifying the carrier phase measurement model in (2.10) to

$$\phi(k) = \left\| \boldsymbol{r}_r(k) - \boldsymbol{r}_{\text{leo}}(k') \right\|_2 + c\Delta\delta t(k) + c\delta t_{\text{iono}}(k) + c\delta t_{\text{tropo}}(k) + v_\phi(k), \tag{3.1}$$

$$c\Delta\delta t(k) \triangleq c\left[\delta t_r(k) - \delta t_{\text{leo}}(k')\right] + \lambda N. \tag{3.2}$$

The process noise covariance associated with the range-equivalent lumped term (3.2) and its

rate of change only depends on the receiver's and LEO SV's stochastic clock error states as the range-equivalent carrier phase ambiguity is deterministic, and is given by

$$\mathbf{Q}_{\text{clk}} = c^2 \left[\mathbf{Q}_{\text{clk},r} + \mathbf{Q}_{\text{clk,leo}}\right], \tag{3.3}$$

where $\mathbf{Q}_{\text{clk},r}$ and $\mathbf{Q}_{\text{clk,leo}}$ are computed from (2.6) by using the receiver's and LEO SV's oscillator power spectra, respectively.

3.3 Experimental Results

To demonstrate the improvements in receiver positioning accuracy and filter consistency, achieved via the adaptation in the IMM over mismatched EKFs, Orbcomm SV signals were collected by a stationary receiver. Orbcomm was chosen for this experiment since its SVs openly transmit ephemeris information in their downlink signals [134]. The ephemeris data was decoded by the receiver and used in the estimators as the SV's ground truth trajectory.

3.3.1 Experimental Setup and Filter Parameters

A very-high frequency (VHF) quadrifilar helix antenna was connected to an Ettus E312 Universal Software Radio Peripheral (USRP) disciplined by a CDA-2990 OctoClock to sample Orbcomm LEO SV signals at 137-138 MHz at a sampling rate of 2.4 MSps.

An IMM estimator and two fixed mismatched EKFs were implemented to estimate the receiver's position and the lumped term (3.2) and its rate of change. It is assumed that the receiver has knowledge of its height (e.g., through altimeter measurements) so that the filters effectively estimate the receiver's planar two-dimensional position in a local North-East-Down (NED) frame.

It is hypothesized that the receiver's clock quality lies between a worst TCXO and a best OCXO and that the LEO SV's clock quality lies between a typical TCXO and a CSAC. As a result, the IMM filter runs $r = 4$ different modes, one for each possible combination of receiver-LEO SV clock quality. The IMM filter is initialized with $\mu_i(0) = 1/r,\ i = 1, \ldots, r$ as no prior is available on the oscillators' stability and the Markovian mode transition matrix is given by $\boldsymbol{\pi}_{ij} = \begin{cases} 1-p, & \text{if } i = j = 1, \ldots, r \\ p/(r-1), & \text{if } i \neq j \end{cases}$ where p is the probability of transition to another mode, which is set to 10^{-4}.

The IMM's performance is also compared to that of two mismatched EKFs: a conservative filter which overbounds $\mathbf{Q}_{\text{clk}}$ by assuming a receiver-LEO SV joint clock quality equivalent to a worst TCXO-typical TCXO pair and an optimistic filter which underestimates $\mathbf{Q}_{\text{clk}}$ by assuming a receiver-LEO SV joint clock quality equivalent to a typical OCXO-best OCXO pair.

3.3.2 Experimental Results

The USRP sampled downlink signals from Orbcomm FM116 SV for around 4.5 minutes. Carrier phase navigation observables were opportunistically extracted by the receiver and were corrected for tropospheric and ionospheric delays using the standard models from Section 2.6. The measurement noise variance was time-varying and was calculated based on the LEO SV's elevation angle. All filters were initialized with the same initial receiver position estimate, drawn from a Gaussian distribution with the mean being the true receiver's location and a variance of 10^6 m^2 in the North and East directions as seen in Fig. 3.2. The initial receiver position error was 1.45 km.

Fig. 3.2 and Table 3.2 summarize the receiver localization performance of the IMM and the two fixed EKFs. Also, the North and East positioning errors and associated $\pm 3\sigma$ bounds

estimated by the IMM and both mismatched fixed EKFs are shown in Fig. 3.3. The following observations can be drawn from these results. First, the IMM yielded better localization performance than the two mismatched EKFs by decreasing the initial positioning error from 1.45 km to 111.26 m versus 254.71 m and 429.35 m for the conservative and optimistic EKFs, respectively. Second, the IMM's covariance captures well the uncertainty in the positioning error whereas the uncertainty for the EKF overbounding $\mathbf{Q}_{\text{clk}}$ is too conservative and the uncertainty for the EKF underestimating $\mathbf{Q}_{\text{clk}}$ is too optimistic. The above observations can be explained by the fact that mismatched process noise covariances lead to less accurate estimates and filter inconsistency or even divergence as in the case of the optimistic EKF [135]. The adaptation capability of the IMM filter addresses the unknown process noise covariance by estimating it online along the receiver position states. Third, the uncertainty ellipses of all three filters are elongated in the same direction as can be seen in Fig. 3.2(a). This is explained by the motion of the LEO SV relative to the receiver: more information is available in the direction parallel to the LEO SV's motion, resulting in more uncertainty (i.e., elongated covariance ellipses) in the direction orthogonal to the LEO SV's trajectory depicted in the skyplot of Fig. 3.2(b).

Fig. 3.4 shows the time evolution of the IMM mode probabilities and suggests that the combined receiver-LEO SV clocks have comparable stability to a typical TCXO-best OCXO oscillator pair.

If a cycle slip occurs in the carrier phase observables, a sharp step equal to the number of cycles slipped multiplied by the carrier wavelength is suddenly introduced in the time evolution of the lumped term (3.2). This step will act as a disturbance to any filter estimating (3.2). It is expected that after the transient period following the cycle slip disturbance, the IMM mode probabilities converge back to the values that correctly characterize the clock error states' process noise covariance.

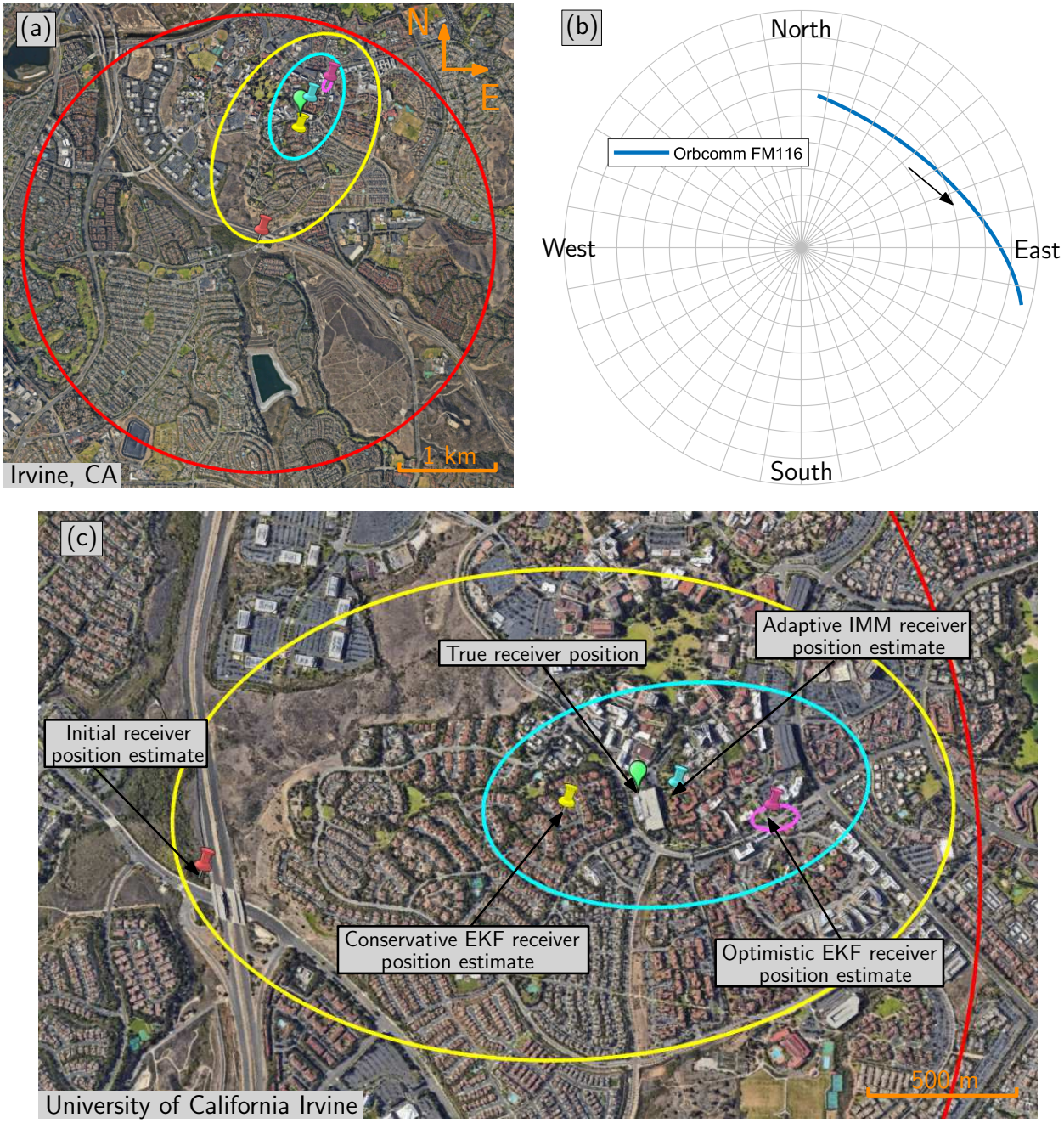

Figure 3.2: (a) Experimental results showing true receiver position (green) along with estimates and corresponding 95^{th}-percentile uncertainty ellipses: (i) red: initial estimate, (ii) yellow: conservative EKF, (iii) purple: optimistic EKF, and (iv) blue: IMM. (b) Skyplot of Orbcomm FM116 SV's trajectory relative to the receiver. (c) Zoomed view on the localization performance of different filters. Map data: Google Earth.

Table 3.2: Comparison of IMM versus mismatched fixed EKFs.

	Adaptive IMM	Conservative EKF	Optimistic EKF
Final 2–D error (m)	111.26	254.71	429.35

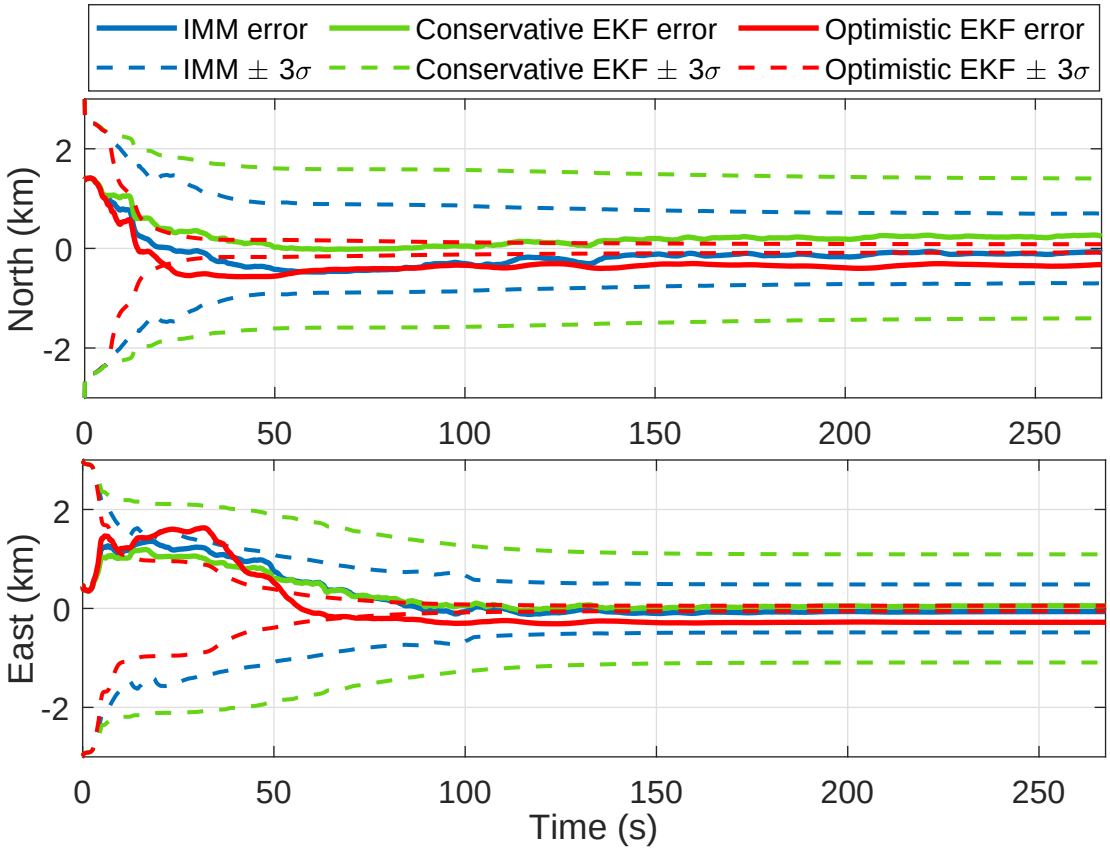

Figure 3.3: North and East receiver positioning errors and associated $\pm 3\sigma$ bounds for the IMM estimator and both mismatched fixed EKFs.

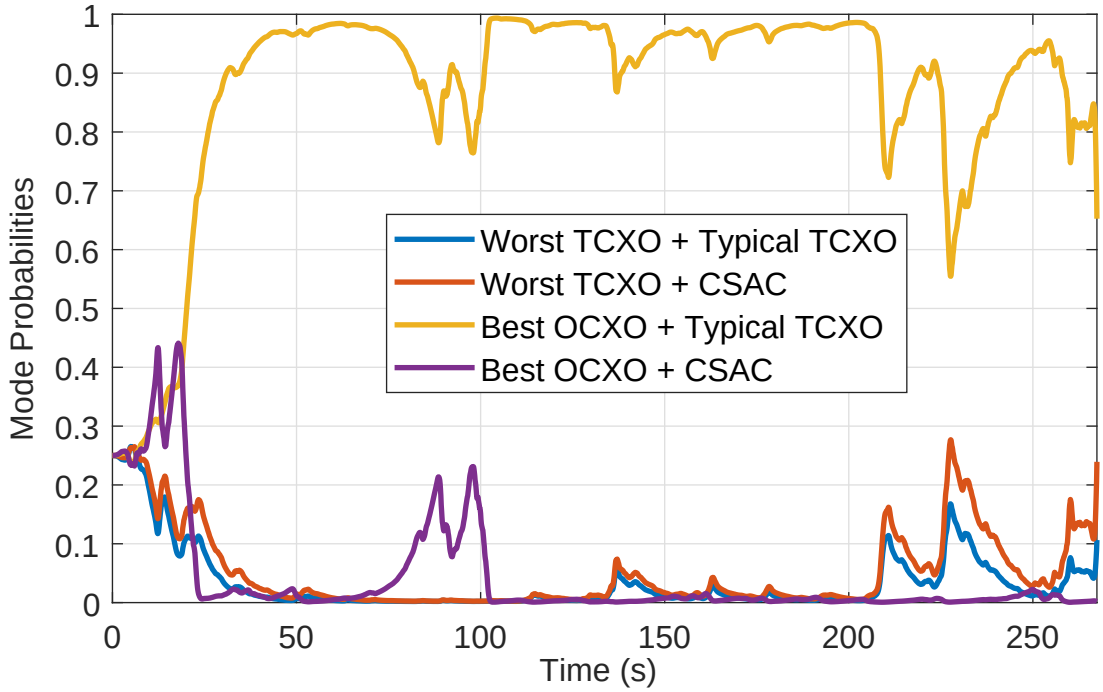

Figure 3.4: IMM mode probabilites.

Chapter 4

Opportunistic LEO Satellite Tracking Framework

This chapter develops a complete tracking framework to refine the LEO SV's ephemeris using navigation observables extracted opportunistically from the LEO SV's downlink signals [136].

4.1 Tracking Filter Formulation

An extended Kalman filter (EKF) is implemented to perform the tracking of LEO SVs by a receiver opportunistically extracting navigation observables from the SV's downlink signals. The state vector estimated by the EKF is

$$\boldsymbol{x} \triangleq \left[\boldsymbol{x}_{\text{leo}}^{\mathsf{T}}, \boldsymbol{x}_{\text{clk}}^{\mathsf{T}}\right]^{\mathsf{T}}, \quad \boldsymbol{x}_{\text{leo}} \triangleq \left[\boldsymbol{r}_{\text{leo}}^{\mathsf{T}}, \dot{\boldsymbol{r}}_{\text{leo}}^{\mathsf{T}}\right]^{\mathsf{T}}$$

$$\boldsymbol{x}_{\text{clk}} \triangleq \left[c\left(\delta t_r - \delta t_{\text{leo}}\right)\ ,\ c\left(\dot{\delta} t_r - \dot{\delta} t_{\text{leo}}\right)\right]^{\mathsf{T}},$$

where $\boldsymbol{r}_{\text{leo}}$ and $\dot{\boldsymbol{r}}_{\text{leo}}$ are the LEO SV's 3-D position and velocity vectors expressed in the ECI reference frame, respectively; and $[\delta t_r - \delta t_{\text{leo}}]$ and $\left[\dot{\delta} t_r - \dot{\delta} t_{\text{leo}}\right]$ are the differences between the receiver's and LEO SV's clock bias and clock drifts, respectively.

The propagation of the LEO SV's position $\boldsymbol{r}_{\text{leo}}$ and velocity $\dot{\boldsymbol{r}}_{\text{leo}}$ is performed by numerical integration of the orbital dynamics equations of motion in (2.3) during the prediction step of the EKF.

4.2 LEO Orbital Motion Process Noise Covariance Characterization

Since the LEO SV's orbital motion process noise covariance matrix $\mathbf{Q}_{\boldsymbol{r}\dot{\boldsymbol{r}}_{\text{leo}}}$ for the SV's Cartesian position and velocity not only affects the uncertainty propagation, but also directly impacts the states' estimates in the tracking filter, it is of critical importance to accurately characterize $\mathbf{Q}_{\boldsymbol{r}\dot{\boldsymbol{r}}_{\text{leo}}}$ before implementing the closed-loop tracking of LEO SVs. To accomplish this, the following methodology based on Monte Carlo simulations is developed:

1. A NORAD-generated publicly available two-line element (TLE) reference file is selected for an Orbcomm LEO SV. The reference TLE epoch as well as the six mean Keplerian elements given at this TLE epoch fully define the orbit of the Orbcomm SV. This reference TLE is propagated for a duration of $K = 6,000$ seconds (i.e., just over one orbital period) with a time-step of one second using the SGP4 propagator and the predicted SV position and velocity are saved in $\boldsymbol{x}_{\boldsymbol{r}\dot{\boldsymbol{r}},\text{ref}}(k),\ k = 1, 2, \ldots, K+1$.

2. $N = 100$ Monte Carlo realizations are created by drawing samples from a Gaussian distribution centered at the reference TLE mean Keplerian elements with a specified covariance matrix that emulates the TLE files' uncertainty at epoch. For each of these

N realizations, a TLE file is generated with the same epoch and corrective terms as the reference TLE but with the randomized mean Keplerian elements.

3. Each of the N randomized TLE realizations of the reference TLE are propagated for $K = 6,000$ seconds with a time-step of one second using the SGP4 propagator and the predicted SV position and velocity $\boldsymbol{x}_{r\dot{r},i}(k)$ are stored at each time-step k for each realization i, where $k = 1, 2, \ldots, K+1$ and $i = 1, 2, \ldots, N$.

4. For each Monte Carlo realization i, the value of the process noise $\boldsymbol{w}_{r\dot{r},i}$ is calculated at each time-step $k = 1, \ldots, K$ according to $\boldsymbol{w}_{r\dot{r},i}(k) = \boldsymbol{x}_{r\dot{r},i}(k+1) - \boldsymbol{f}_{r\dot{r}}\left(\boldsymbol{x}_{r\dot{r},i}(k)\right)$, where $\boldsymbol{f}_{r\dot{r}}$ is the nonlinear SV dynamics propagation model used in the filter's prediction step.

5. The empirical covariance $\mathbf{Q}_{r\dot{r},\text{emp}}$ of the process noise is computed at each time-step k by averaging $\boldsymbol{w}_{r\dot{r},i}(k)\boldsymbol{w}_{r\dot{r},i}^{\mathsf{T}}(k)$ across Monte Carlo realizations according to $\mathbf{Q}_{r\dot{r},\text{emp}}(k) = \frac{1}{N}\sum_{i=1}^{N} \boldsymbol{w}_{r\dot{r},i}(k)\boldsymbol{w}_{r\dot{r},i}^{\mathsf{T}}(k),\ k = 1, \ldots, K.$

Since both the SGP4 propagation $\boldsymbol{x}_{r\dot{r},i}(k+1)$ and the filter's prediction $\boldsymbol{f}_{r\dot{r}}\left(\boldsymbol{x}_{r\dot{r},i}(k)\right)$ are performed in the ECI reference frame, the process noise vectors $\boldsymbol{w}_{r\dot{r},i}(k)$ are also expressed in the ECI frame. As a result, $\mathbf{Q}_{r\dot{r},\text{emp}}(k)$ will be the empirical process noise covariance at each time-step expressed in the ECI frame.

To provide a more intuitive interpretation of the effect of the process noise on the LEO SV's motion, the rotation matrix $\mathbf{R}_i^b$ from the ECI frame, denoted $\{i\}$, to the SV's body frame (along-track, cross-track, and radial directions), denoted $\{b\}$, is computed at each time-step k and the empirical process noise covariance determined by the Monte Carlo analysis described above ${}^{i}\mathbf{Q}_{r\dot{r},\text{emp}}(k)$ is rotated to form ${}^{b}\mathbf{Q}_{r\dot{r},\text{emp}}(k),\ k = 1, 2, \ldots, K.$

In addition to providing a more intuitive and visual interpretation of the process noise, ${}^{b}\mathbf{Q}_{r\dot{r},\text{emp}}$ is also more invariant than ${}^{i}\mathbf{Q}_{r\dot{r},\text{emp}}$ since in the SV's body frame, the SV's motion is constrained to be in the along-track – radial plane (orbital plane) with the velocity in

the along-track direction and with no motion in the cross-track direction; whereas in the ECI frame, the LEO SV's motion has generally components in all directions which are time-varying as the SV orbits Earth. Moreover, the invariance brought by the expression of the process noise covariance matrix in the SV's body frame allows for a generalization of ${}^{b}\mathbf{Q}_{\boldsymbol{r}\dot{\boldsymbol{r}},\text{emp}}$ to all LEO SVs, which have similar motion characteristics in the body frame, while ${}^{i}\mathbf{Q}_{\boldsymbol{r}\dot{\boldsymbol{r}},\text{emp}}$ would only be applicable for the reference SV chosen in the Monte Carlo framework at a specific time determined by the SV's position in the ECI frame. To further enhance the generalization of the process noise covariance matrix, the invariance of ${}^{b}\mathbf{Q}_{\boldsymbol{r}\dot{\boldsymbol{r}},\text{emp}}$ is leveraged to define ${}^{b}\bar{\mathbf{Q}}_{\boldsymbol{r}\dot{\boldsymbol{r}},\text{emp}} \triangleq \frac{1}{K}\sum_{k=1}^{K} {}^{b}\mathbf{Q}_{\boldsymbol{r}\dot{\boldsymbol{r}},\text{emp}}(k)$, which will be used in the LEO SV tracking filter. The 95^{th}-percentile error ellipsoid associated with the LEO SV's position states (i.e, top-left 3×3 block of ${}^{b}\bar{\mathbf{Q}}_{\boldsymbol{r}\dot{\boldsymbol{r}},\text{emp}}$) can be visualized in Fig. 4.1(a).

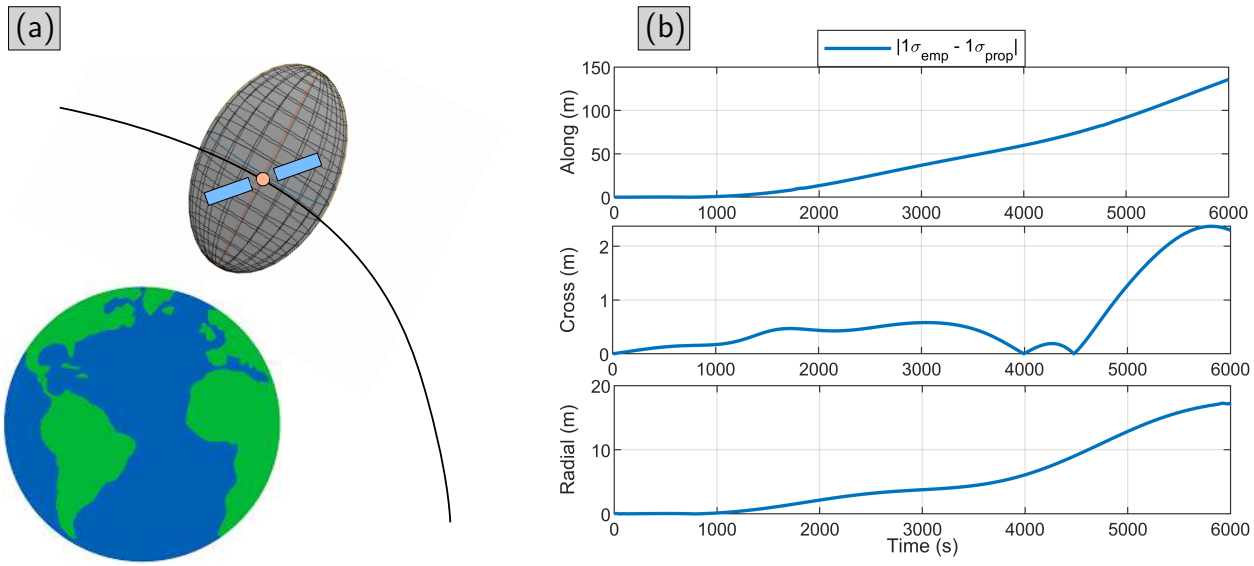

Figure 4.1: (a) Visualization of the 95^{th}-percentile error ellipsoid of the averaged process noise covariance characterized for one orbital period in the body frame for the LEO SV's position states. (b) Absolute difference between the empirical and propagated LEO SV position states standard deviations in the LEO SV's body frame over 100 minutes.

To validate this methodology, the empirical position and velocity covariance matrix ${}^{i}\mathbf{P}_{\boldsymbol{r}\dot{\boldsymbol{r}},\text{emp}}(k) = \frac{1}{N}\sum_{i=1}^{N} \tilde{\boldsymbol{x}}_{\boldsymbol{r}\dot{\boldsymbol{r}},i}(k)\tilde{\boldsymbol{x}}_{\boldsymbol{r}\dot{\boldsymbol{r}},i}^{\mathsf{T}}(k)$, where $\tilde{\boldsymbol{x}}_{\boldsymbol{r}\dot{\boldsymbol{r}},i}(k) \triangleq \boldsymbol{x}_{\boldsymbol{r}\dot{\boldsymbol{r}},\text{ref}}(k) - \boldsymbol{x}_{\boldsymbol{r}\dot{\boldsymbol{r}},i}(k)$, is computed from the Monte Carlo runs of SGP4 propagation of the different TLE realizations. In parallel, the open-loop filter propagation of the initial empirical position and velocity covariance matrix ${}^{i}\mathbf{P}_{\boldsymbol{r}\dot{\boldsymbol{r}},\text{emp}}(1)$

is computed using ${}^{b}\bar{\mathbf{Q}}_{\boldsymbol{r}\dot{\boldsymbol{r}},\text{emp}}$ to account for the process noise of the SV's position and velocity states and is denoted by ${}^{i}\mathbf{P}_{\boldsymbol{r}\dot{\boldsymbol{r}},\text{prop}}(k)$. ${}^{b}\bar{\mathbf{Q}}_{\boldsymbol{r}\dot{\boldsymbol{r}},\text{emp}}$ was rotated at each time-step k using the current rotation matrix $\mathbf{R}_{b}^{i}(k)$ to form ${}^{i}\bar{\mathbf{Q}}_{\boldsymbol{r}\dot{\boldsymbol{r}},\text{emp}}(k)$ and perform the propagation of ${}^{i}\mathbf{P}_{\boldsymbol{r}\dot{\boldsymbol{r}},\text{prop}}$ in the ECI frame. Finally, the absolute difference between the empirical and propagated position standard deviations is plotted in Fig. 4.1(b) in the LEO SV's body frame for $k = 1, \ldots, K+1$.

The following observations can be made. First, note that the error ellipsoid of the LEO SV's position states process noise covariance matrix is mostly elongated in the radial direction as can be seen from Fig. 4.1(a). This can be explained by the fact that most of the acceleration perturbations are in this direction and are mainly caused by the unmodeled non-uniformity of Earth's gravitational potential beyond the J_2 term. Second, the absolute difference between the empirical and propagated LEO SV position states standard deviations is the largest for the along-track axis, revealing that the LEO SV position process noise covariance was the least well matched in this direction. Nevertheless, the absolute difference for the position in the along-track axis is lower than 150 m after more than one orbit of open-loop covariance propagation around Earth. Additionally, for time spans of less than 10 minutes during which a LEO SV is typically visible to a receiver, this absolute difference is very small and is a sign that the LEO SV orbital motion process noise covariance characterization developed in this section is accurate enough for LEO SV opportunistic navigation.

4.3 Simulation Results

4.3.1 Simulation Setup and Settings

A comprehensive Monte Carlo simulation is performed to study the efficacy of opportunistic LEO SV tracking using 3 different sets of observables: (i) pseudorange measurements, (ii)

Doppler measurements, and (iii) fused pseudorange and Doppler measurements. In this simulation, 103 SVs with diverse elevation profiles and geometries relative to the receiver, as depicted in the skyplot in Fig. 4.2, are tracked with each set of measurements at a rate of 1 Hz for a duration of 5 minutes. Additionally, for each of the 103 SVs, 100 Monte Carlo runs are simulated resulting in a total of 10,300 tracking runs for each set of observables. In each Monte Carlo run, the initial SV's position and velocity is obtained from a randomized TLE, which is generated with realistic errors consistent with uncertainties observed in NORAD-published TLEs. Moreover, the time evolution of the receiver's and LEO SVs' clock error states as well as the measurement noise are randomized for each Monte Carlo run. The simulation setup and randomization settings are presented next.

Receiver and LEO Satellites' Trajectories

The tracking receiver was simulated to be stationary with a known location on the University of California Irvine (UCI) campus.

The FCC-approved 12,000-satellite Starlink LEO constellation was simulated using orbital parameters found in the FCC filings. The LEO SV' trajectories were obtained through SGP4 propagations of simulated TLEs for the 12,000 Starlink satellite megaconstellation. The elevation angle mask was set to 10°.

Clock Error States

The receiver was assumed to be equipped with a typical-quality oven-controlled crystal oscillator (OCXO) and the LEO SVs were assumed to have best-quality OCXOs. The power-law coefficients of these oscillators are given in Table 4.1 and can be used to compute the discrete-time process noise covariance for the clock error states $\mathbf{Q}_{\text{clk},r}$ and $\mathbf{Q}_{\text{clk,leo}}$ from (2.6). The clock bias and drift of the LEO receiver and LEO SV transmitters were simulated accord-

ing to the standard two-state clock error model (2.5). The values of the receiver's clock error states $\boldsymbol{x}_{\text{clk},r}(0) \triangleq \left[c\delta t_r(0), c\dot{\delta} t_r(0)\right]$ were initialized as $\boldsymbol{x}_{\text{clk},r}(0) \sim \mathcal{N}\left[\mathbf{0}_{2\times 1}, \mathbf{P}_{\text{clk},r}\right]$, where $\mathbf{P}_{\text{clk},r} = \text{diag}\left[9 \times 10^4, 9 \times 10^{-2}\right]$ with units of [m^2, (m/s)^2] corresponding to a 1σ of 1 μs and 1 ns/s for the clock bias and drift, respectively. The values of the LEO SVs' clock error states $\boldsymbol{x}_{\text{clk,leo}}(0) \triangleq \left[c\delta t_{\text{leo}}(0), c\dot{\delta} t_{\text{leo}}(0)\right]$ were initialized as $\boldsymbol{x}_{\text{clk,leo}}(0) \sim \mathcal{N}\left[\mathbf{0}_{2\times 1}, \mathbf{P}_{\text{clk,leo}}\right]$, where $\mathbf{P}_{\text{clk,leo}} = \text{diag}\left[9 \times 10^2, 9 \times 10^{-4}\right]$ with units of [m^2, (m/s)^2] corresponding to a 1σ of 0.1 μs and 0.1 ns/s for the clock bias and drift, respectively.

Table 4.1: Receiver's and LEO SVs' oscillator parameters.

Quality	**Coefficients $\{\boldsymbol{h_0}, \boldsymbol{h_{-2}}\}$**
Receiver's typical-quality OCXO	$\{8.0 \times 10^{-20}, 4.0 \times 10^{-23}\}$
LEO SVs' best-quality OCXO	$\{2.6 \times 10^{-22}, 4.0 \times 10^{-26}\}$

Measurements

Pseudorange navigation observables to all visible LEO SVs were generated according to (2.7). The time-varying pseudorange measurement noise variances were calculated from the predicted carrier-to-noise C/N_0, which was found from the log-distance path loss model

$$(C/N_0)_l(k) = P_0 - 10\log_{10}\left(d_l(k)/D_0\right), \tag{4.1}$$

where $P_0 = 56$ dB-Hz is the nominal C/N_0 at a distance $D_0 = 1,000$ km and $d_l(k) \triangleq \left\|\boldsymbol{r}_r(k) - \boldsymbol{r}_{\text{leo},l}(k)\right\|_2$ is the distance between the receiver and the l-th LEO SV. The pseudorange measurement noise variances are proportional to the square root of the inverse of C/N_0, expressed in linear units, and ranged between 0.43 and 3.73 m^2.

Pseudorange rate measurements to all visible LEO SVs were generated according to (2.9). Pseudorange rate measurements are directly proportional to Doppler frequency observables as demonstrated in (2.8) but are independent of the carrier frequency. As a result, pseudo-

range rate measurements were preferred over Doppler to obtain comparable measurements from different constellations which transmit downlink signals at frequencies that are orders of magnitude apart. The time-varying pseudorange rate measurement noise variances are proportional to the square root of the inverse of C/N_0 from (4.1), expressed in linear units, and ranged between 0.13 and 1.17 $(\mathrm{m/s})^2$, based on the distance between the receiver and the SVs.

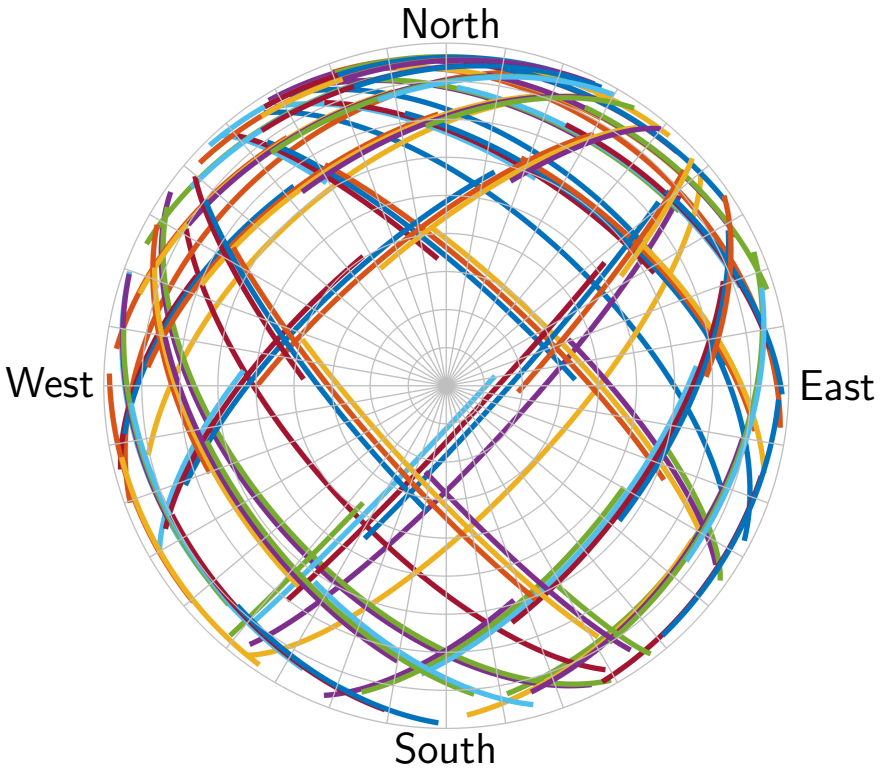

Figure 4.2: Skyplot of 103 SVs tracked in Monte Carlo simulation.

4.3.2 Filter Initialization

The l-th LEO SV position and velocity state estimates $\hat{\boldsymbol{x}}_{\boldsymbol{r}\dot{\boldsymbol{r}}_{\text{leo},l}}(0|0) \triangleq \left[\hat{\boldsymbol{r}}^{\mathsf{T}}_{\text{leo},l}(0|0), \hat{\dot{\boldsymbol{r}}}^{\mathsf{T}}_{\text{leo},l}(0|0)\right]^{\mathsf{T}}$ were initialized in the ECI frame, denoted by $\{i\}$, as follows

$$
\begin{aligned}
&\hat{\boldsymbol{x}}_{\boldsymbol{r}\dot{\boldsymbol{r}}_{\text{leo},l}}(0|0) \sim \mathcal{N}\left[\boldsymbol{x}_{\boldsymbol{r}\dot{\boldsymbol{r}}_{\text{leo},l}}(0),\, \mathbf{P}_{\boldsymbol{x}_{\boldsymbol{r}\dot{\boldsymbol{r}}_{\text{leo},l}}}(0|0)\right] \\
&\mathbf{P}_{\boldsymbol{x}_{\boldsymbol{r}\dot{\boldsymbol{r}}_{\text{leo},l}}}(0|0) \triangleq \text{diag}\left[\mathbf{P}_{\boldsymbol{x}_{\boldsymbol{r}_{\text{leo},l}}}(0|0), \mathbf{P}_{\boldsymbol{x}_{\dot{\boldsymbol{r}}_{\text{leo},l}}}(0|0)\right] \\
&\mathbf{P}_{\boldsymbol{x}_{\boldsymbol{r}_{\text{leo},l}}}(0|0) = \mathbf{R}^{i}_{b_{\text{leo},l}}(0)\, {}^{b_{\text{leo}}}\mathbf{P}_{\boldsymbol{x}_{\boldsymbol{r}_{\text{leo}}}}(0|0) \left[\mathbf{R}^{i}_{b_{\text{leo},l}}(0)\right]^{\mathsf{T}} \\
&\mathbf{P}_{\boldsymbol{x}_{\dot{\boldsymbol{r}}_{\text{leo},l}}}(0|0) = \mathbf{R}^{i}_{b_{\text{leo},l}}(0)\, {}^{b_{\text{leo}}}\mathbf{P}_{\boldsymbol{x}_{\dot{\boldsymbol{r}}_{\text{leo}}}}(0|0) \left[\mathbf{R}^{i}_{b_{\text{leo},l}}(0)\right]^{\mathsf{T}},
\end{aligned}
$$

where $\boldsymbol{x}_{\boldsymbol{r}\dot{\boldsymbol{r}}_{\text{leo},l}}(0)$ is the l-th LEO SV's true position and velocity states in ECI and $\mathbf{P}_{\boldsymbol{x}_{\boldsymbol{r}\dot{\boldsymbol{r}}_{\text{leo},l}}}(0|0)$ is the associated initial covariance; ${}^{b_{\text{leo}}}\mathbf{P}_{\boldsymbol{x}_{\boldsymbol{r}_{\text{leo}}}}(0|0) \triangleq \text{diag}\left[4 \times 10^{6}, 10^{2}, 10^{4}\right]$ m^2 and ${}^{b_{\text{leo}}}\mathbf{P}_{\boldsymbol{x}_{\dot{\boldsymbol{r}}_{\text{leo}}}}(0|0) \triangleq \text{diag}\left[4 \times 10^{-2}, 10^{-4}, 4\right]$ (m/s)^2 are the initial LEO SV's position and velocity covariances in the SV's body frame $\{b_{\text{leo}}\}$, respectively; and $\mathbf{R}^{i}_{b_{\text{leo},l}}(0)$ is the initial rotation matrix from the l-th LEO SV's body frame $\{b_{\text{leo}_l}\}$ to the ECI frame $\{i\}$. The first entry of the LEO SV's position and velocity covariances in the SV's body frame corresponds to the SVs' along-track axis, the second entry is associated with the cross-track direction, and the last entry is for the radial axis. These values were carefully selected to closely match the uncertainties inherent to TLE files with the most uncertainty being in the along-track position and radial velocity, while the cross-track direction TLE errors are the least substantial as the SVs' motion is constrained in the orbital (along-track – radial) plane.

The LEO SVs' position and velocity states process noise covariance ${}^{b}\bar{\mathbf{Q}}_{\boldsymbol{r}\dot{\boldsymbol{r}},\text{emp}}$ found from the methodology in Section 4.2 was used in the EKF to account for the effect of unmodeled uncertainties in the LEO SVs' orbital motion. This process noise covariance matrix expressed in the SV's body frame was rotated to the ECI frame at each EKF time update step for every LEO SV. Note that time-step of 1 second chosen in Section 4.2 is consistent with the propagation time-step in the EKF as the measurement updates are performed at a rate

of 1 Hz.

The filter's clock error states $\boldsymbol{x}_{\text{clk}}(0|0)$ were initialized as $\boldsymbol{x}_{\text{clk}}(0|0) \sim \mathcal{N}\left[\mathbf{0}_{2\times 1}, \mathbf{P}_{\text{clk}}(0|0)\right]$, where $\mathbf{P}_{\text{clk}}(0|0) = \mathbf{P}_{\text{clk},r} + \mathbf{P}_{\text{clk,leo}}$. The process noise covariance for the filter's clock error states is set to $\mathbf{Q}_{\text{clk}} = c^2\left[\mathbf{Q}_{\text{clk},r} + \mathbf{Q}_{\text{clk,leo}}\right]$.

4.3.3 Monte Carlo Tracking Results

The Monte Carlo tracking simulation results for the 3 observable sets: (i) pseudorange measurements, (ii) Doppler measurements, and (iii) fused pseudorange and Doppler measurements are presented in this section.

The EKF tracked position and velocity root mean-squared errors (RMSEs) were computed for each SV by averaging over the ensemble of 100 Monte Carlo realizations performed for each SV. These position and velocity RMSEs were then averaged over all the 103 SVs tracked in the simulation. Furthermore, open-loop SGP4 propagations of the randomized TLE, which served to initialize the EKF's initial position and velocity estimates, were performed for each Monte Carlo realization. The average performance of SGP4 is computed in a similar fashion to the EKF tracking one: an ensemble average over the Monte Carlo realizations for each SV which is then averaged over all SVs. Figs. 4.3 and 4.4 respectively show the position and velocity RMSEs expressed in the body frame of the open-loop SGP4-propagated ephemerides as well as the ephemerides tracked using the 3 different set of observables: (i) pseudorange measurements, (ii) Doppler measurements, and (iii) fused pseudorange and Doppler measurements. The magnitude of the LEO SV position error for the open-loop SGP4 propagation and the tracking using the 3 measurement sets is shown in Fig. 4.5.

This comprehensive Monte Carlo study reveals the average performance of the opportunistic LEO tracking framework presented in this chapter. The following remarks and observations

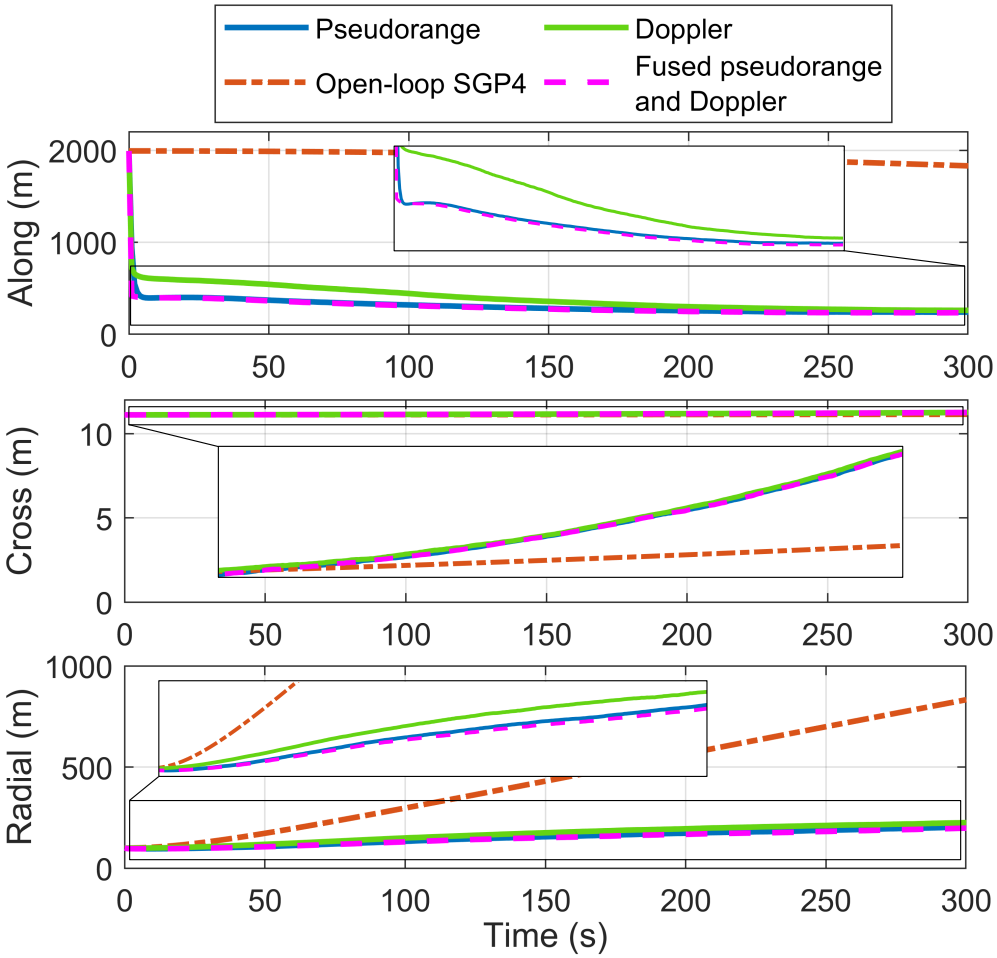

Figure 4.3: Position RMSEs for tracking using pseudorange, Doppler, and fused pseudorange and Doppler versus SGP4's open-loop position RMSE.

can be made from these simulations. First, the location of the stationary tracking receiver can be chosen arbitrarily without loss of generality. This is supported by the fact that no location is more favorable than another if Earth is assumed to be a sphere. The main difference observed with a different receiver location would be the number of visible SVs, which depends on the receiver's latitude and LEO SV constellation parameters (i.e., inclination of orbital planes). Second, since the LEO SV tracking is performed in the ECI frame, the receiver's position and velocity is also found in the ECI frame by converting the stationary Earth-centered, Earth-fixed (ECEF) position while accounting for Earth's rotation, nutation and precession effects, and polar motion. Third, it can be seen that the cross-track direction is the least observable for both position and velocity states. This can be explained by the

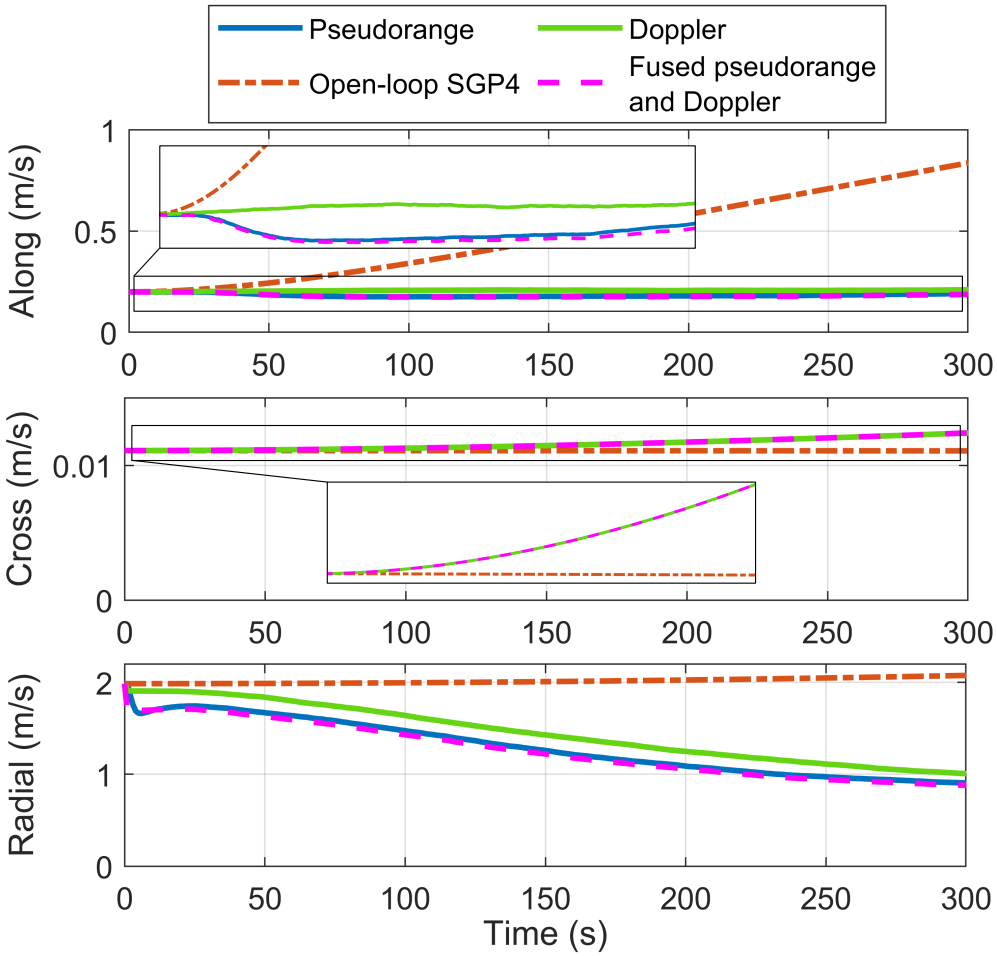

Figure 4.4: Velocity RMSEs for tracking using pseudorange, Doppler, and fused pseudorange and Doppler versus SGP4's open-loop velocity RMSE.

fact that the SV's motion is restricted in the along-track–radial plane. As a result, the cross-track direction is not excited during the SV's motion, which leads to poor estimability of the corresponding states. Fourth, it can be seen from Figs. 4.3-4.5 that using pseudorange measurements yield better LEO SV tracking performance than Doppler measurements. Fifth, fusing both pseudorange and Doppler measurements yields negligible improvements over pseudorange-only tracking. This is suggested by the fact that both types of measurements are highly correlated, thus leading to a negligible information increase when augmenting the pseudorange measurement vector to include both navigation observables. Sixth, it is worth noting that the clock bias term $c\,[\delta t_r - \delta t_{\text{leo}}]$ is unobservable with Doppler measurements only and is consequently not estimated during LEO SV tracking with this set of observables.

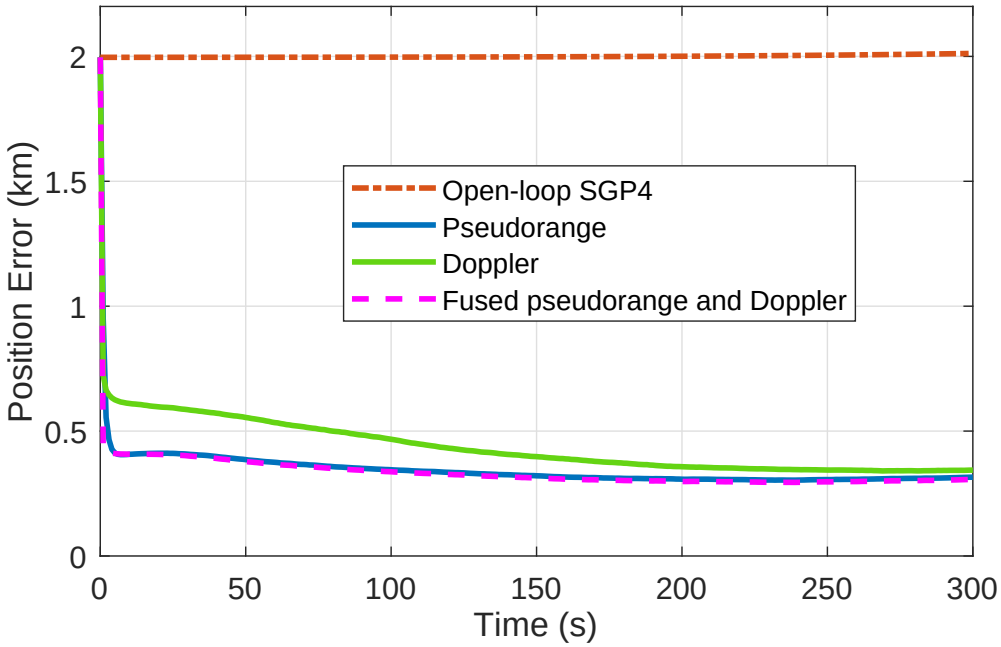

Figure 4.5: Magnitude of position error for tracking using pseudorange, Doppler, and fused pseudorange and Doppler versus SGP4's open-loop position error.

4.4 Experimental Results

This section presents the results of an experiment performed with a stationary receiver on the UCI campus opportunistically extracting carrier phase navigation observables from an Orbcomm LEO SV's downlink signals. The Orbcomm LEO constellation was chosen for this experiment as Orbcomm SVs openly transmit ephemeris information obtained from their on-board GPS receivers in their downlink signals [134]. As a result, the receiver can decode this accurate ephemeris information which will serve as a ground truth to assess the performance of the LEO SV tracking framework developed in this chapter in comparison to the open-loop SPG4-propagated TLE ephemeris.

4.4.1 Experimental Setup and Filter Settings

A very-high frequency (VHF) antenna was connected to an Ettus E312 Universal Software Radio Peripheral (USRP) to receive Orbcomm downlink signals at 137-138 MHz and sample

them at 2.4 MSps. The USRP's oscillator was driven by an external, freely-running CDA-2990 OctoClock. Carrier phase navigation observables were opportunistically extracted by the receiver and were corrected for ionospheric and tropospheric effects using the standard models from Section 2.6. These measurements were then filtered at a rate of 1 Hz in the EKF developed in Section 4.1 to perform the tracking of the Orbcomm FM107 SV. The tracking was performed for around 6 minutes and the skyplot of the Orbcomm SV trajectory during the experiment is shown in Fig. 4.8(b).

The LEO SV's position and velocity estimates were initialized from the SGP4-propagated ephemeris of the most recent TLE available for the Orbcomm FM107 SV tracked in this experiment. The associated initial position and velocity covariances were set to ${}^{b}\mathbf{P}_{\boldsymbol{x}_{\boldsymbol{r}}}(0|0) \triangleq \text{diag}\left[10^{7}, 10^{3}, 10^{4}\right]$ m^2 and ${}^{b}\mathbf{P}_{\boldsymbol{x}_{\dot{\boldsymbol{r}}}}(0|0) \triangleq \text{diag}\left[10^{-2}, 10^{-1}, 10^{2}\right]$ (m/s)^2 in the SV's body frame, respectively. Since carrier phase measurements are used in this experiment, the clock bias difference term of $\boldsymbol{x}_{\text{clk}}$ is modified by adding the carrier phase ambiguity term from (2.10) and becomes (3.2). This term is initialized by subtracting the initial estimated range from the first carrier phase measurement. The clock drift term was initialized to 0 and the clock error states' covariance was initialized to $\mathbf{P}_{\boldsymbol{x}_{\text{clk}}} \triangleq \text{diag}\left[10^{7}, 10^{2}\right]$ with units of [m^2, (m/s)^2] corresponding to a 1σ of around 11 μs and 33 ns/s for the clock bias and drift, respectively.

The process noise covariance of the Orbcomm SV's orbital motion was set to be ${}^{b}\bar{\mathbf{Q}}_{\boldsymbol{r}\dot{\boldsymbol{r}},\text{emp}}$ found in Section 4.2 since the update rate of the EKF was set to 1 Hz. Moreover, ${}^{b}\bar{\mathbf{Q}}_{\boldsymbol{r}\dot{\boldsymbol{r}},\text{emp}}$ was rotated to the ECI frame at each time-step to propagate the estimation error covariance of the LEO SV's position and velocity states. The process noise covariance of the clock error states was set to be equivalent to a combination of a typical temperature-compensated crystal oscillator (TCXO)-best OCXO pair. The power-law coefficients of these oscillators are given in Table 4.2 and can be used to compute the discrete-time process noise covariance for the clock error states $\mathbf{Q}_{\text{clk}}$. This choice was motivated by the findings of Chapter 3 that characterized the combined oscillators' quality for the clock on-board Orbcomm SVs and

the CDA-2990 OctoClock used to discipline the receiver's clock in this experiment. The time-varying measurement noise was set to be proportional to the inverse of the predicted C/N_0 from (4.1) expressed in linear units and ranged between 3.49 and 4.84 m^2.

Table 4.2: Experimental oscillator parameters.

Quality	**Coefficients** $\{\boldsymbol{h_0}, \boldsymbol{h_{-2}}\}$
Typical TCXO	$\{9.4 \times 10^{-20}, 3.8 \times 10^{-21}\}$
Best OCXO	$\{2.6 \times 10^{-22}, 4.0 \times 10^{-26}\}$

4.4.2 Experimental Tracking Results

Figs. 4.6 and 4.7 respectively show the position and velocity EKF error plots and associated $\pm 3\sigma$ bounds as well as the open-loop SGP4-propagated ephemeris errors in the SV's body frame. The initial position and velocity errors of over 7.1 km and 7.3 m/s obtained from the SGP4 propagation of the most recent TLE of the Orbcomm FM107 SV were reduced to final errors of 698.7 m and 1.81 m/s, respectively, in just over 6 minutes of tracking.

The following are key takeaways and remarks from these experimental tracking results. First, note that the LEO SV tracking performance with carrier phase observables is similar to that using pseudorange measurements as both measurement models only differ by the carrier phase ambiguity (2.7)-(2.10) and the effect of the ionosphere on the measurements: δt_{iono} acts as delay for pseudoranges and as an advance for carrier phases. After correcting for the atmospheric effects, accounting for the carrier phase ambiguity term is done by lumping it with the clock bias difference term and estimating the resulting term (3.2) in the filter. Second, as can be seen from Figs. 4.6 and 4.7, the open-loop SGP4-propagated ephemeris errors stay constant over the entire experiment. Moreover, opportunistic tracking mostly reduces the along-track position and radial velocity errors, which are usually where most of the errors in ephemerides obtained from TLEs lie. The radial position and along-track

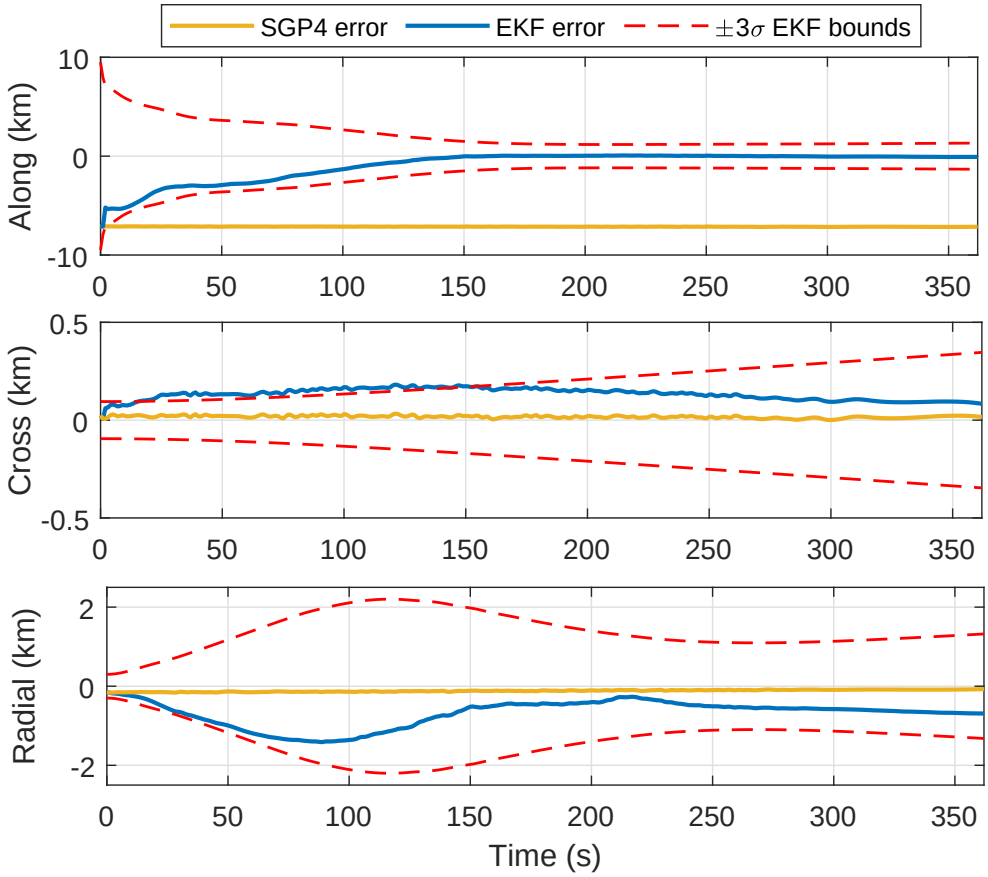

Figure 4.6: EKF-tracked position errors with associated $\pm 3\sigma$ bounds versus open-loop SGP4 errors for Orbcomm FM107 SV.

velocity errors, however, increase slightly during tracking as compared to their open-loop SGP4 counterparts. Third, as demonstrated in simulations in Subsection 4.3.3, the cross-track direction is verified experimentally to be the least observable for both position and velocity. Fourth, note that the oscillations observed in the Orbcomm SV's velocity EKF plots in Fig. 4.7 between 0 and 30 seconds are due to the noisy decoding of the ground truth ephemeris information transmitted by the SV in its downlink signals. This happens at the beginning of the tracking period as the Orbcomm SV's elevation is still low (below 16° before 30 seconds), thus leading to errors in the ephemeris packet decoding as a result of the low carrier-to-noise ratio.

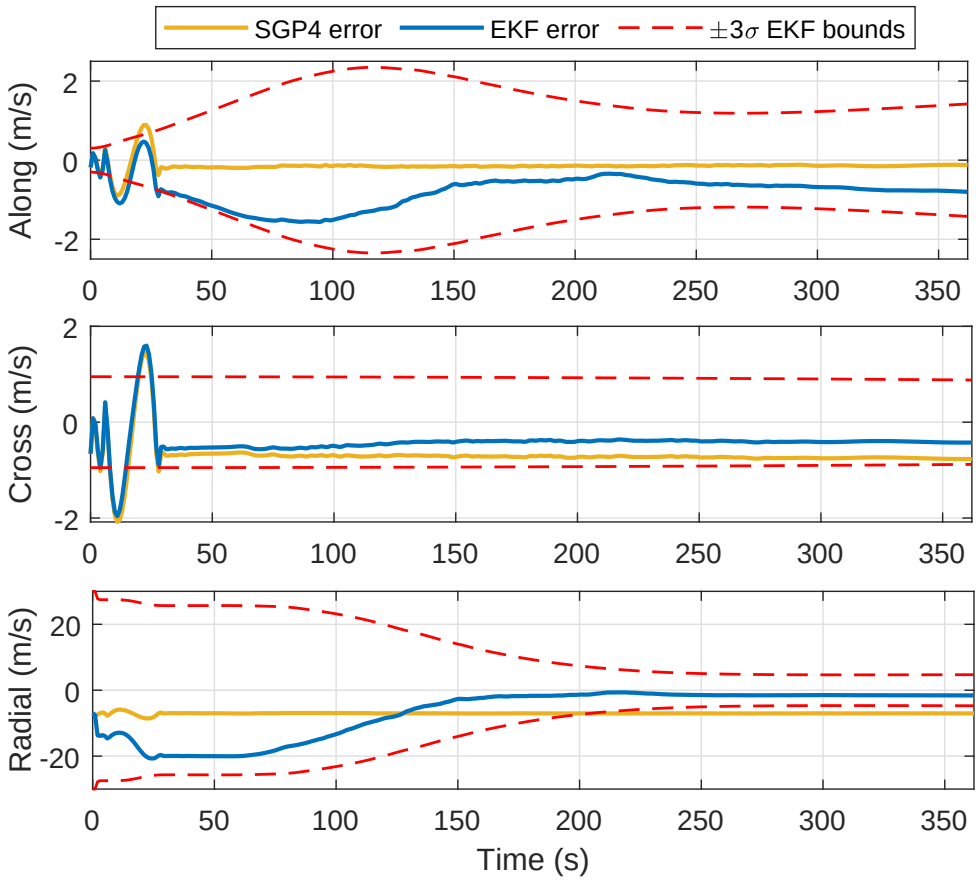

Figure 4.7: EKF-tracked velocity errors with associated $\pm 3\sigma$ bounds versus open-loop SGP4 errors for Orbcomm FM107 SV.

4.4.3 Experimental Receiver Localization Results

To demonstrate the practical advantages of LEO SV ephemeris refinement via the opportunistic tracking framework presented in this chapter, an EKF is implemented to localize the stationary receiver using the open-loop SGP4-propagated ephemeris on one hand and the refined ephemeris resulting from the tracking performed in Subsection 4.4.2 on the other hand. It is assumed that the receiver has knowledge of its height (e.g., through altimeter measurements) so that the filters effectively estimate the receiver's horizontal 2-D position in a local East-North-Up (ENU) frame.

The state vector estimated by the EKF is $\boldsymbol{x} \triangleq \left[\boldsymbol{r}_r^{\mathsf{T}}, \boldsymbol{x}_{\text{clk}}^{\mathsf{T}}\right]$, where $\boldsymbol{r}_r$ is the receiver' 3-D position in the ECEF reference frame and $\boldsymbol{x}_{\text{clk}}^{\mathsf{T}}$ is the same as in Subsection 4.4.2 with the carrier

phase ambiguity term added to the clock bias difference. Since the fixed ECEF position of the receiver is estimated, the Orbcomm SV's ephemeris is also computed in the ECEF frame, denoted $\{e\}$. The TLE-generated ephemeris ${}^{e}\boldsymbol{x}_{\text{leo,SGP4}}$ is computed by performing the SGP4 propagations of the most recent TLE for the Orbcomm FM107 SV in the ECEF frame. The refined ephemeris is obtained by propagating backward in time the last tracked position and velocity estimate in the ECI frame by numerical integration of the two-body with J_2 equations of motion (2.3). This is done to obtain a smoothed trajectory for the tracked SV's motion in the ECI frame, which is then rotated to ECEF to yield ${}^{e}\boldsymbol{x}_{\text{leo,tracked}}$.

Both EKFs were initialized with the same initial receiver position estimate, drawn from a Gaussian distribution with the mean being the true receiver's location and a variance of 10^8 m^2 in the East and North directions as seen in Fig. 4.8(a). The initial receiver position error was 13.48 km. The clock error states' covariance was initialized to $\mathbf{P}_{\boldsymbol{x}_{\text{clk}}} \triangleq \text{diag}\,[10^8, 10^2]$ with units of [m^2, $(\text{m/s})^2$] corresponding to a 1σ of around 33 μs and 33 ns/s for the clock bias and drift, respectively. The clock error states process noise covariance and time-varying measurement noise were identical to those in Subsection 4.4.2.

The experimental localization results are shown in Fig. 4.8 and Table 4.3 and are summarized next. The 2-D positioning error of the receiver localized using the refined tracked ephemeris ${}^{e}\boldsymbol{x}_{\text{leo,tracked}}$ was decreased from its initial value of around 13.48 km to 343.47 m while the localization performed using the SGP4-propagated ephemeris ${}^{e}\boldsymbol{x}_{\text{leo,SGP4}}$ diverged to over 6.85 km in error. The inconsistency of the localization estimate using the ${}^{e}\boldsymbol{x}_{\text{leo,SGP4}}$ is due to a clear model mismatch as the SGP4-propagated ephemeris fed to the EKF is over 7.13 km away from the true SV's ephemeris on average and is a sign of filter divergence [135]. Additionally, note that the shape, size, and orientation of the uncertainty ellipses of both EKFs in Fig. 4.8(c) are similar. This is explained by both EKFs having the same initial estimation error covariance, process noise covariance, time-varying measurement noise and the fact that the measurement Jacobians of both EKFs are nearly identical: the time history

of the unit line-of-sight (LOS) vectors pointing from the SV to the estimated receiver location are very close for both ${}^{e}\boldsymbol{x}_{\text{leo,tracked}}$ and ${}^{e}\boldsymbol{x}_{\text{leo,SGP4}}$.

Table 4.3: Horizontal 2–D positioning errors for EKF using open-loop SGP4-propagated ephemeris and EKF using refined tracked ephemeris.

	Initial	Final (SGP4 ephemeris)	Final (refined ephemeris)
Horizontal error (m)	13,476	6,852	343.47

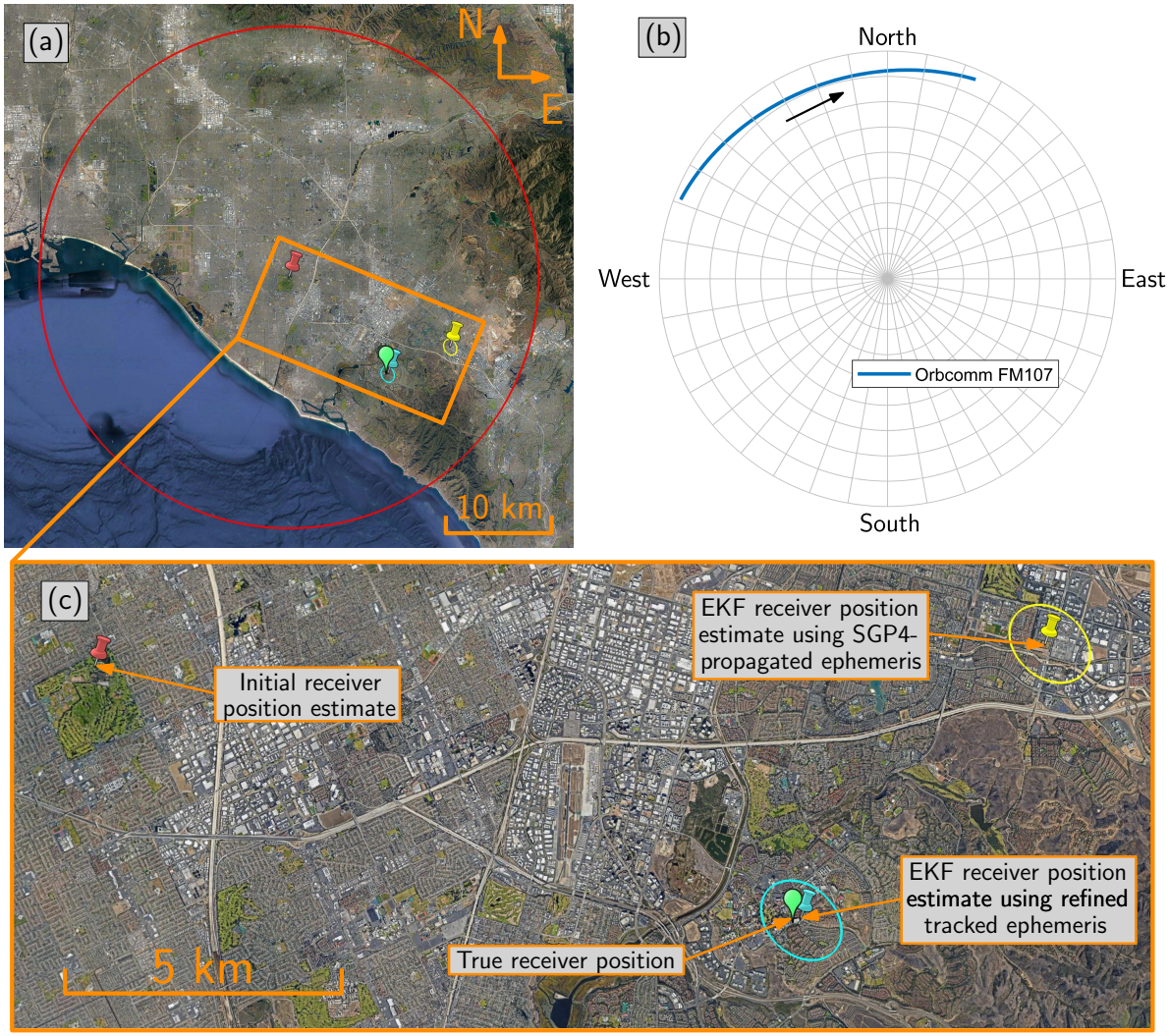

Figure 4.8: (a) Experimental results showing true receiver position (green) along with estimates and corresponding 95^{th}-percentile horizontal uncertainty ellipses: (i) red: initial estimate, (ii) yellow: EKF using ${}^{e}\boldsymbol{x}_{\text{leo,SGP4}}$ ephemeris, and (iii) blue: EKF using ${}^{e}\boldsymbol{x}_{\text{leo,tracked}}$ ephemeris. (b) Skyplot of Orbcomm FM107 SV's trajectory relative to the receiver. (c) Zoomed view on the localization performance of both EKFs. Map data: Google Earth.

Chapter 5

Conclusions

This thesis presented a complete study on the opportunistic estimation of LEO satellites' states to enable LEO-based opportunistic navigation. The unknown clock error states with unknown process noise covariance (as no information is available on the oscillator quality on-board LEO SVs) and the uncertainty in the TLE-generated ephemerides challenges were tackled. An interacting multiple-model (IMM) estimator was first developed to adaptively estimate the stability of the combined receiver-LEO SV clocks online while localizing the receiver. Next, the opportunistic tracking of LEO SVs was comprehensively studied: a methodology to characterize the LEO SVs' orbital motion process noise covariance was proposed and extensive Monte Carlo simulations were performed to compare the performance of the tracking filter with three sets of measurements. Experimental results with Orbcomm LEO SVs were presented to demonstrate the efficacy of the estimators developed in this thesis to unlock the potential of LEO-based navigation.

Bibliography

[1] J. Du and M. Barth, "Next-generation automated vehicle location systems: Positioning at the lane level," *IEEE Transactions on Intelligent Transportation Systems*, vol. 9, no. 1, pp. 48–57, March 2008.

[2] M. Uijt de Haag, E. Dill, S. Young, and M. Joerger, "Position, navigation, and timing technologies in the 21st century," J. Morton, F. van Diggelen, J. Spilker, Jr., and B. Parkinson, Eds. Wiley-IEEE, 2021, vol. 2, ch. 60: Commercial Unmanned Aircraft Systems (UAS), pp. 1171–1223.

[3] Z. Kassas, P. Closas, and J. Gross, "Navigation systems for autonomous and semi-autonomous vehicles: Current trends and future challenges," *IEEE Aerospace and Electronic Systems Magazine*, vol. 34, no. 5, pp. 82–84, May 2019.

[4] R. Ioannides, T. Pany, and G. Gibbons, "Known vulnerabilities of global navigation satellite systems, status, and potential mitigation techniques," *Proceedings of the IEEE*, vol. 104, no. 6, pp. 1174–1194, February 2016.

[5] D. Miralles, A. Bornot, P. Rouquette, N. Levigne, D. Akos, Y.-H.Chen, S. Lo, and T. Walter, "An assessment of GPS spoofing detection via radio power and signal quality monitoring for aviation safety operations," *IEEE Intelligent Transportation Systems Magazine*, vol. 12, no. 3, pp. 136–146, June 2020.

[6] M. Leng, F. Quitin, W. Tay, C. Cheng, S. Razul, and C. See, "Anchor-aided joint localization and synchronization using SOOP: Theory and experiments," *IEEE Transactions on Wireless Communications*, vol. 15, no. 11, pp. 7670–7685, November 2016.

[7] J. del Peral-Rosado, R. Estatuet-Castillo, J. Lopez-Salcedo, G. Seco-Granados, Z. Chaloupka, L. Ries, and J. Garcoa-Molina, "Evaluation of hybrid positioning scenarios for autonomous vehicle applications," in *Proceedings of ION International Technical Meeting Conference*, January 2017, pp. 2541–2553.

[8] Z. Kassas, J. Morales, K. Shamaei, and J. Khalife, "LTE steers UAV," *GPS World Magazine*, vol. 28, no. 4, pp. 18–25, April 2017.

[9] Z. Kassas, J. Khalife, K. Shamaei, and J. Morales, "I hear, therefore I know where I am: Compensating for GNSS limitations with cellular signals," *IEEE Signal Processing Magazine*, pp. 111–124, September 2017.

[10] A. Coluccia and A. Fascista, "A review of advanced localization techniques for crowd-sensing wireless sensor networks," *Sensors*, vol. 19, no. 5, pp. 988–1017, 2019.

[11] J. Russell, M. Ye, B. Anderson, H. Hmam, and P. Sarunic, "Cooperative localization of a GPS-denied UAV using direction-of-arrival measurements," *IEEE Transactions on Aerospace and Electronic Systems*, vol. 56, no. 3, pp. 1966–1978, June 2020.

[12] Z. Kassas, M. Maaref, J. Morales, J. Khalife, and K. Shamaei, "Robust vehicular localization and map matching in urban environments through IMU, GNSS, and cellular signals," *IEEE Intelligent Transportation Systems Magazine*, vol. 12, no. 3, pp. 36–52, June 2020.

[13] Z. Kassas, J. Khalife, M. Neinavaie, and T. Mortlock, "Opportunity comes knocking: overcoming GPS vulnerabilities with other satellites' signals," *Inside Unmanned Systems Magazine*, pp. 30–35, June/July 2020.

[14] J. Mortier, G. Pages, and J. Vila-Valls, "Robust TOA-based UAS navigation under model mismatch in GNSS-denied harsh environments," *Remote Sensing*, vol. 12, no. 18, pp. 2928–2947, September 2020.

[15] Q. Shi, X. Cui, S. Zhao, S. Xu, and M. Lu, "BLAS: Broadcast relative localization and clock synchronization for dynamic dense multiagent systems," *IEEE Transactions on Aerospace and Electronic Systems*, vol. 56, no. 5, pp. 3822–3839, October 2020.

[16] L. Zhong, R. Wang, Y. Wang, Y. Ni, X. Liu, and L. Wang, "Optimizing INS/GNSS/UWB integrated vehicle collaboration navigation based on performance analysis under crowded environments," in *Proceedings of International Conference on Unmanned Systems*, November 2020, pp. 1042–1046.

[17] Z. Wang, R. Liu, Q. Liu, L. Han, and J. Thompson, "Feasibility study of UAV-assisted anti-jamming positioning," *IEEE Transactions on Vehicular Technology*, vol. 70, no. 8, pp. 7718–7733, August 2021.

[18] Z. Kassas, J. Khalife, A. Abdallah, and C. Lee, "I am not afraid of the GPS jammer: resilient navigation via signals of opportunity in GPS-denied environments," *IEEE Aerospace and Electronic Systems Magazine*, 2022, accepted.

[19] Z. Kassas, "Collaborative opportunistic navigation," *IEEE Aerospace and Electronic Systems Magazine*, vol. 28, no. 6, pp. 38–41, 2013.

[20] Z. Kassas and T. Humphreys, "Observability analysis of collaborative opportunistic navigation with pseudorange measurements," *IEEE Transactions on Intelligent Transportation Systems*, vol. 15, no. 1, pp. 260–273, February 2014.

[21] J. Raquet *et al.*, "Position, navigation, and timing technologies in the 21st century," J. Morton, F. van Diggelen, J. Spilker, Jr., and B. Parkinson, Eds. Wiley-IEEE, 2021, vol. 2, Part D: Position, Navigation, and Timing Using Radio Signals-of-Opportunity, ch. 35–43, pp. 1115–1412.

[22] N. Souli, P. Kolios, and G. Ellinas, "Online relative positioning of autonomous vehicles using signals of opportunity," *IEEE Transactions on Intelligent Vehicles*, pp. 1–1, 2021.

[23] J. McEllroy, "Navigation using signals of opportunity in the AM transmission band," Master's thesis, Air Force Institute of Technology, Wright-Patterson Air Force Base, Ohio, USA, 2006.

[24] X. Chen, Q. Wei, F. Wang, Z. Jun, S. Wu, and A. Men, "Super-resolution time of arrival estimation for a symbiotic FM radio data system," *IEEE Transactions on Broadcasting*, vol. 66, no. 4, pp. 847–856, December 2020.

[25] C. Yang, T. Nguyen, and E. Blasch, "Mobile positioning via fusion of mixed signals of opportunity," *IEEE Aerospace and Electronic Systems Magazine*, vol. 29, no. 4, pp. 34–46, April 2014.

[26] L. Chen, O. Julien, P. Thevenon, D. Serant, A. Pena, and H. Kuusniemi, "TOA estimation for positioning with DVB-T signals in outdoor static tests," *IEEE Transactions on Broadcasting*, vol. 61, no. 4, pp. 625–638, 2015.

[27] J. del Peral-Rosado, R. Raulefs, J. Lopez-Salcedo, and G. Seco-Granados, "Survey of cellular mobile radio localization methods: from 1G to 5G," *IEEE Communications Surveys & Tutorials*, vol. 20, no. 2, pp. 1124–1148, 2018.

[28] Z. Kassas, "Position, navigation, and timing technologies in the 21st century," J. Morton, F. van Diggelen, J. Spilker, Jr., and B. Parkinson, Eds. Wiley-IEEE, 2021, vol. 2, ch. 38: Navigation with Cellular Signals of Opportunity, pp. 1171–1223.

[29] J. Khalife and Z. Kassas, "Navigation with cellular CDMA signals – part II: Performance analysis and experimental results," *IEEE Transactions on Signal Processing*, vol. 66, no. 8, pp. 2204–2218, April 2018.

[30] K. Shamaei and Z. Kassas, "LTE receiver design and multipath analysis for navigation in urban environments," *NAVIGATION, Journal of the Institute of Navigation*, vol. 65, no. 4, pp. 655–675, December 2018.

[31] P. Gadka, J. Sadowski, and J. Stefanski, "Detection of the first component of the received LTE signal in the OTDoA method," *Wireless Communications and Mobile Computing*, pp. 1–12, April 2019.

[32] S. Han, T. Kang, and J. Seo, "Smartphone application to estimate distances from LTE base stations based on received signal strength measurements," in *International Technical Conference on Circuits/Systems, Computers and Communications*, June 2019, pp. 1–3.

[33] T. Kang, H. Lee, and J. Seo, "TOA-based ranging method using CRS in LTE signals," *Journal of Advanced Navigation Technology*, vol. 23, no. 5, pp. 437–443, October 2019.

[34] J. Gante, L. Sousa, and G. Falcao, "Dethroning GPS: Low-power accurate 5G positioning systems using machine learning," *IEEE Journal on Emerging and Selected Topics in Circuits and Systems*, vol. 10, no. 2, pp. 240–252, June 2020.

[35] P. Wang and Y. Morton, "Multipath estimating delay lock loop for LTE signal TOA estimation in indoor and urban environments," *IEEE Transactions on Wireless Communications*, vol. 19, no. 8, pp. 5518–5530, 2020.

[36] H. Dun, C. Tiberius, and G. Janssen, "Positioning in a multipath channel using OFDM signals with carrier phase tracking," *IEEE Access*, vol. 8, pp. 13 011–13 028, 2020.

[37] K. Shamaei and Z. Kassas, "A joint TOA and DOA acquisition and tracking approach for positioning with LTE signals," *IEEE Transactions on Signal Processing*, pp. 2689–2705, 2021.

[38] K. Shamaei and Z. Kassas, "Receiver design and time of arrival estimation for opportunistic localization with 5G signals," *IEEE Transactions on Wireless Communications*, vol. 20, no. 7, pp. 4716–4731, 2021.

[39] T. Kazaz, G. Janssen, J. Romme, and A. Van der Veen, "Delay estimation for ranging and localization using multiband channel state information," *IEEE Transactions on Wireless Communications*, pp. 1–16, September 2021.

[40] M. Driusso, C. Marshall, M. Sabathy, F. Knutti, H. Mathis, and F. Babich, "Vehicular position tracking using LTE signals," *IEEE Transactions on Vehicular Technology*, vol. 66, no. 4, pp. 3376–3391, April 2017.

[41] J. Khalife and Z. Kassas, "Precise UAV navigation with cellular carrier phase measurements," in *Proceedings of IEEE/ION Position, Location, and Navigation Symposium*, April 2018, pp. 978–989.

[42] J. Morales and Z. Kassas, "Stochastic observability and uncertainty characterization in simultaneous receiver and transmitter localization," *IEEE Transactions on Aerospace and Electronic Systems*, vol. 55, no. 2, pp. 1021–1031, April 2019.

[43] J. del Peral-Rosado, O. Renaudin, C. Gentner, R. Raulefs, E. Dominguez-Tijero, A. Fernandez-Cabezas, F. Blazquez-Luengo, G. Cueto-Felgueroso, A. Chassaigne, D. Bartlett, F. Grec, L. Ries, R. Prieto-Cerdeira, J. Lopez-Salcedo, and G. Seco-Granados, "Physical-layer abstraction for hybrid GNSS and 5G positioning evaluations," in *Proceedings of IEEE Vehicular Technology Conference*, September 2019, pp. 1–6.

[44] K. Shamaei and Z. Kassas, "Sub-meter accurate UAV navigation and cycle slip detection with LTE carrier phase," in *Proceedings of ION GNSS Conference*, September 2019, pp. 2469–2479.

[45] Z. Kassas, J. Khalife, A. Abdallah, and C. Lee, "I am not afraid of the jammer: navigating with signals of opportunity in GPS-denied environments," in *Proceedings of ION GNSS Conference*, 2020, pp. 1566–1585.

[46] J. Khalife and Z. Kassas, "Opportunistic UAV navigation with carrier phase measurements from asynchronous cellular signals," *IEEE Transactions on Aerospace and Electronic Systems*, vol. 56, no. 4, pp. 3285–3301, August 2020.

[47] M. Maaref and Z. Kassas, "Measurement characterization and autonomous outlier detection and exclusion for ground vehicle navigation with cellular signals," *IEEE Transactions on Intelligent Vehicles*, vol. 5, no. 4, pp. 670–683, December 2020.

[48] A. Abdallah and Z. Kassas, "UAV navigation with 5G carrier phase measurements," in *Proceedings of ION GNSS Conference*, September 2021, pp. 3294–3306.

[49] G. Afifi and Y. Gadallah, "Autonomous 3-D UAV localization using cellular networks: Deep supervised learning versus reinforcement learning approaches," *IEEE Access*, vol. 9, pp. 155 234–155 248, 2021.

[50] Z. Kassas, A. Abdallah, and M. Orabi, "Carpe signum: seize the signal – opportunistic navigation with 5G," *Inside GNSS Magazine*, vol. 16, no. 1, pp. 52–57, 2021.

[51] J. Khalife and Z. Kassas, "On the achievability of submeter-accurate UAV navigation with cellular signals exploiting loose network synchronization," *IEEE Transactions on Aerospace and Electronic Systems*, 2022, accepted.

[52] R. Landry, A. Nguyen, H. Rasaee, A. Amrhar, X. Fang, and H. Benzerrouk, "Iridium Next LEO satellites as an alternative PNT in GNSS denied environments–part 1," *Inside GNSS Magazine*, vol. 14, no. 3, pp. 56–64., May 2019.

[53] S. Thompson, S. Martin, and D. Bevly, "Single differenced Doppler positioning with low Earth orbit signals of opportunity and angle of arrival estimation," in *Proceedings of ION International Technical Meeting*, 2020, pp. 497–509.

[54] T. Reid, B. Chan, A. Goel, K. Gunning, B. Manning, J. Martin, A. Neish, A. Perkins, and P. Tarantino, "Satellite navigation for the age of autonomy," in *Proceedings of IEEE/ION Position, Location and Navigation Symposium*, 2020, pp. 342–352.

[55] J. Khalife, M. Neinavaie, and Z. Kassas, "Navigation with differential carrier phase measurements from megaconstellation LEO satellites," in *Proceedings of IEEE/ION Position, Location, and Navigation Symposium*, April 2020, pp. 1393–1404.

[56] Q. Wei, X. Chen, and Y. Zhan, "Exploring implicit pilots for precise estimation of LEO satellite downlink Doppler frequency," *IEEE Communications Letters*, vol. 24, no. 10, pp. 2270–2274, 2020.

[57] A. Nardin, F. Dovis, and J. Fraire, "Empowering the tracking performance of LEO-based positioning by means of meta-signals," *IEEE Journal of Radio Frequency Identification*, vol. 5, no. 3, pp. 244–253, 2021.

[58] P. Iannucci and T. Humphreys, "Fused low-Earth-orbit GNSS," *arXiv.org*, 2021, (submitted to IEEE Transactions on Aerospace and Electronics Systems).

[59] M. Psiaki, "Navigation using carrier Doppler shift from a LEO constellation: TRANSIT on steroids," *NAVIGATION, Journal of the Institute of Navigation*, vol. 68, no. 3, pp. 621–641, September 2021.

[60] Z. Kassas, M. Neinavaie, J. Khalife, N. Khairallah, J. Haidar-Ahmad, S. Kozhaya, and Z. Shadram, "Enter LEO on the GNSS stage: Navigation with Starlink satellites," *Inside GNSS Magazine*, vol. 16, no. 6, pp. 42–51, 2021.

[61] R. Cassel, D. Scherer, D. Wilburne, J. Hirschauer, and J. Burke, "Impact of improved oscillator stability on LEO-based satellite navigation," in *Proceedings of ION International Technical Meeting*, January 2022, pp. 893–905.

[62] J. Khalife, M. Neinavaie, and Z. Kassas, "The first carrier phase tracking and positioning results with Starlink LEO satellite signals," *IEEE Transactions on Aerospace and Electronic Systems*, vol. 56, no. 2, pp. 1487–1491, April 2022.

[63] B. Mclemore and M. Psiaki, "Navigation using doppler shift from LEO constellations and INS data," *IEEE Transactions on Aerospace and Electronic Systems*, 2022.

[64] T. Reid, T. Walter, P. Enge, D. Lawrence, H. Cobb, G. Gutt, M. O'Conner, and D. Whelan, "Position, navigation, and timing technologies in the 21st century," J. Morton, F. van Diggelen, J. Spilker, Jr., and B. Parkinson, Eds. Wiley-IEEE, 2021, vol. 2, ch. 43: Navigation from low Earth orbit – Part 1: Concept, Current Capability, and Future Promise, pp. 1359–1379.

[65] Z. Kassas, "Position, navigation, and timing technologies in the 21st century," J. Morton, F. van Diggelen, J. Spilker, Jr., and B. Parkinson, Eds. Wiley-IEEE, 2021, vol. 2, ch. 43: Navigation from low Earth orbit – Part 2: models, implementation, and performance, pp. 1381–1412.

[66] Union of Concerned Scientists, "UCS satellite database," https://www.ucsusa.org/resources/satellite-database, January 2022.

[67] S. Liu, Z. Gao, Y. Wu, D. Kwan Ng, X. Gao, K. Wong, S. Chatzinotas, and B. Ottersten, "LEO satellite constellations for 5G and beyond: How will they reshape vertical domains?" *IEEE Communications Magazine*, vol. 59, no. 7, pp. 30–36, July 2021.

[68] T. Reid, "Orbital diversity of global navigation satellite systems," Ph.D. dissertation, Stanford University, USA, 2017.

[69] D. Lawrence, H. Cobb, G. Gutt, M. OConnor, T. Reid, T. Walter, and D. Whelan, "Navigation from LEO: Current capability and future promise," *GPS World Magazine*, vol. 28, no. 7, pp. 42–48, July 2017.

[70] L. Gill, D. Grenier, and J. Chouinard, "Use of XM radio satellite signal as a source of opportunity for passive coherent location," *IET Radar, Sonar Navigation*, vol. 5, no. 5, pp. 536–544, June 2011.

[71] J. Khalife and Z. Kassas, "Receiver design for Doppler positioning with LEO satellites," in *Proceedings of IEEE International Conference on Acoustics, Speech and Signal Processing*, May 2019, pp. 5506–5510.

[72] Z. Tan, H. Qin, L. Cong, and C. Zhao, "New method for positioning using IRIDIUM satellite signals of opportunity," *IEEE Access*, vol. 7, pp. 83 412–83 423, 2019.

[73] F. Farhangian and R. Landry, "Multi-constellation software-defined receiver for Doppler positioning with LEO satellites," *Sensors*, vol. 20, no. 20, pp. 5866–5883, October 2020.

[74] M. Orabi, J. Khalife, and Z. Kassas, "Opportunistic navigation with Doppler measurements from Iridium Next and Orbcomm LEO satellites," in *Proceedings of IEEE Aerospace Conference*, March 2021, pp. 1–9.

[75] C. Pinell, "Receiver architectures for positioning with low Earth orbit satellite signals," Master's thesis, Lulea University of Technology, School of Electrical Engineering, Sweden, 2021.

[76] M. Neinavaie, J. Khalife, and Z. Kassas, "Cognitive opportunistic navigation in private networks with 5G signals and beyond," *IEEE Journal of Selected Topics in Signal Processing*, 2021, accepted.

[77] M. Neinavaie, J. Khalife, and Z. Kassas, "Blind opportunistic navigation: Cognitive deciphering of partially known signals of opportunity," in *Proceedings of ION GNSS Conference*, September 2020, pp. 2748–2757.

[78] J. Khalife, M. Neinavaie, and Z. Kassas, "Blind Doppler estimation from LEO satellite signals: A case study with real 5G signals," in *Proceedings of ION GNSS Conference*, September 2020, pp. 3046–3054.

[79] M. Neinavaie, J. Khalife, and Z. Kassas, "Blind Doppler tracking and beacon detection for opportunistic navigation with LEO satellite signals," in *Proceedings of IEEE Aerospace Conference*, March 2021, pp. 1–8.

[80] J. Khalife, M. Neinavaie, and Z. Kassas, "Blind Doppler tracking from OFDM signals transmitted by broadband LEO satellites," in *Proceedings of IEEE Vehicular Technology Conference*, April 2021, pp. 1–6.

[81] M. Neinavaie, J. Khalife, and Z. Kassas, "Doppler stretch estimation with application to tracking Globalstar satellite signals," in *Proceedings of IEEE Military Communications Conference*, November 2021, pp. 647–651.

[82] M. Neinavaie, J. Khalife, and Z. Kassas, "Acquisition, Doppler tracking, and positioning with Starlink LEO satellites: First results," *IEEE Transactions on Aerospace and Electronic Systems*, 2021, accepted.

[83] Z. Kassas, J. Morales, and J. Khalife, "New-age satellite-based navigation – STAN: simultaneous tracking and navigation with LEO satellite signals," *Inside GNSS Magazine*, vol. 14, no. 4, pp. 56–65, 2019.

[84] T. Mortlock and Z. Kassas, "Performance analysis of simultaneous tracking and navigation with LEO satellites," in *Proceedings of ION GNSS Conference*, September 2020, pp. 2416–2429.

[85] North American Aerospace Defense Command (NORAD), "Two-line element sets," http://celestrak.com/NORAD/elements/.

[86] D. Vallado and P. Crawford, "SGP4 orbit determination," in *Proceedings of AIAA/AAS Astrodynamics Specialist Conference and Exhibit*, August 2008, pp. 6770–6799.

[87] D. Vallado, "An analysis of state vector propagation using differing flight dynamics programs," in *Proceedings of the AAS Space Flight Mechanics Conference*, vol. 120, January 2005, pp. 1563–1592.

[88] "Analytical Graphics, Inc., Systems Tool Kit (STK)," https://www.agi.com/products/stk.

[89] Systems Tool Kit (STK), "High-Precision Orbit Propagator (HPOP)," https://help.agi.com/stk/11.0.1/Content/hpop/hpop.htm, September 2016.

[90] P. Cefola, J. San-Juan, S. Setty, and R. Proulx, "Review of the Draper semi-analytical satellite theory (DSST)," in *Proceedings of 18th Australian International Aerospace Congress*, 2019.

[91] O. Montenbruck and E. Gill, *Satellite orbits: models, methods, and applications*. Springer, 2000.

[92] B. Schutz, B. Tapley, and G. Born, *Statistical orbit determination*. Elsevier, 2004.

[93] USSTRATCOM, "U.S. Strategic Command Fact Sheet Combined Space Operations Center / 614th Air Operations Center," https://www.stratcom.mil/Portals/8/Documents/CSpOC_Factsheet_2018.pdf, July 2018.

[94] S. Sharma and J. Cutler, "Robust orbit determination and classification: A learning theoretic approach," *IPN Progress Report*, pp. 42–203, 2015.

[95] B. Lee, W. Kim, J. Lee, and Y. Hwang, "Machine learning approach to initial orbit determination of unknown LEO satellites," in *Proceedings of AIAA SpaceOps Conference*, 2018, pp. 1–11.

[96] D. Shen, J. Lu, G. Chen, E. Blasch, C. Sheaff, M. Pugh, and K. Pham, "Methods of machine learning for space object pattern classification," in *Proceedings of IEEE National Aerospace and Electronics Conference*, 2019, pp. 565–572.

[97] H. Peng and X. Bai, "Comparative evaluation of three machine learning algorithms on improving orbit prediction accuracy," *Astrodynamics*, vol. 3, no. 4, pp. 325–343, 2019.

[98] H. Peng and X. Bai, "Machine learning approach to improve satellite orbit prediction accuracy using publicly available data," *The Journal of the Astronautical Sciences*, vol. 67, no. 2, pp. 762–793, 2020.

[99] B. Li, J. Huang, Y. Feng, F. Wang, and J. Sang, "A machine learning-based approach for improved orbit predictions of LEO space debris with sparse tracking data from a single station," *IEEE Transactions on Aerospace and Electronic Systems*, vol. 56, no. 6, pp. 4253–4268, 2020.

[100] T. Mortlock and Z. Kassas, "Assessing machine learning for LEO satellite orbit determination in simultaneous tracking and navigation," in *Proceedings of IEEE Aerospace Conference*, March 2021, pp. 1–8.

[101] S. Kozhaya, J. Haidar-Ahmad, A. Abdallah, Z. Kassas, and S. Saab, "Comparison of neural network architectures for simultaneous tracking and navigation with LEO satellites," in *Proceedings of ION GNSS Conference*, September 2021, pp. 2507–2520.

[102] J. Haidar-Ahmad, N. Khairallah, and Z. Kassas, "A hybrid analytical-machine learning approach for LEO satellite orbit prediction," in *Proceedings of International Conference on Information Fusion*, 2022, accepted.

[103] J. Vetter, "Fifty years of orbit determination: Development of modern astrodynamics methods," *Johns Hopkins APL Technical Digest*, vol. 27, no. 3, pp. 239–252, November 2007.

[104] B. Tapley, M. Watkins, C. Ries, W. Davis, R. Eanes, S. Poole, H. Rim, B. Schutz, C. Shum, R. Nerem, F. Lerch, J. Marshall, S. Klosko, N. Pavlis, and R. Williamson, "The Joint Gravity Model 3," *Journal of Geophysical Research*, vol. 101, no. B12, pp. 28 029–28 049, December 1996.

[105] J. Vinti, *Orbital and Celestial Mechanics*. American Institute of Aeronautics and Astronautics, 1998.

[106] J. Morales, J. Khalife, U. Santa Cruz, and Z. Kassas, "Orbit modeling for simultaneous tracking and navigation using LEO satellite signals," in *Proceedings of ION GNSS Conference*, September 2019, pp. 2090–2099.

[107] R. Brown and P. Hwang, *Introduction to Random Signals and Applied Kalman Filtering*, 3rd ed. John Wiley & Sons, 2002.

[108] A. Thompson, J. Moran, and G. Swenson, *Interferometry and Synthesis in Radio Astronomy*, 2nd ed. John Wiley & Sons, 2001.

[109] Y. Bar-Shalom, X. Li, and T. Kirubarajan, *Estimation with Applications to Tracking and Navigation*. New York, NY: John Wiley & Sons, 2002.

[110] P. Misra and P. Enge, *Global Positioning System: Signals, Measurements, and Performance*, 2nd ed. Ganga-Jamuna Press, 2010.

[111] NASA JPL, "Ionospheric and atmospheric remote sensing," https://iono.jpl.nasa.gov/.

[112] NASA, "NASA's archive of space geodesy data," https://cddis.nasa.gov/archive/gnss/products/ionex/.

[113] N. Khairallah and Z. Kassas, "An interacting multiple model estimator of LEO satellite clocks for improved positioning," in *Proceedings of IEEE Vehicular Technology Conference*, 2022, accepted.

[114] J. Duník, O. Straka, O. Kost, and J. Havlík, "Noise covariance matrices in state-space models: a survey and comparison of estimation methods – part I," *International Journal of Adaptive Control and Signal Processing*, vol. 31, no. 11, pp. 1505–1543, 2017.

[115] R. Shumway and D. Stoffer, "An approach to time series smoothing and forecasting using the EM algorithm," *Journal of Time Series Analysis*, vol. 3, no. 4, pp. 253–264, July 1982.

[116] J. Dunik, O. Straka, and M. Simandl, "On autocovariance least-squares method for noise covariance matrices estimation," *IEEE Transactions on Automatic Control*, vol. 62, no. 2, pp. 967–972, February 2017.

[117] B. Odelson, M. Rajamani, and J. Rawlings, "A new autocovariance least-squares method for estimating noise covariances," *Automatica*, vol. 42, no. 2, pp. 303–308, 2006.

[118] K. Myers and B. Tapley, "Adaptive sequential estimation with unknown noise statistics," *IEEE Transactions on Automatic Control*, vol. 21, no. 4, pp. 520–523, 1976.

[119] N. Stacey and S. D'Amico, "Adaptive and dynamically constrained process noise estimation for orbit determination," *IEEE Transactions on Aerospace and Electronic Systems*, vol. 57, no. 5, pp. 2920–2937, October 2021.

[120] A. Moghaddamjoo and K. Lynn, "Robust adaptive kalman filtering," in *Approximate Kalman Filtering*. World Scientific, 1993, pp. 65–85.

[121] X. Li and Y. Bar-Shalom, "Multiple-model estimation with variable structure," *IEEE Transactions on Automatic Control*, vol. 41, no. 4, pp. 478–493, August 1996.

[122] W. Ouyang, Y. Wu, and H. Chen, "INS/Odometer land navigation by accurate measurement modeling and multiple-model adaptive estimation," *IEEE Transactions on Aerospace and Electronic Systems*, vol. 57, no. 1, pp. 245–262, 2021.

[123] M. Gomaa, O. De Silva, G. Mann, and G. Gosine, "Observability-constrained VINS for MAVs using interacting multiple model algorithm," *IEEE Transactions on Aerospace and Electronic Systems*, vol. 57, no. 3, pp. 1423–1442, June 2021.

[124] L. Xu, X. Li, and Z. Duan, "Hybrid grid multiple-model estimation with application to maneuvering target tracking," *IEEE Transactions on Aerospace and Electronic Systems*, vol. 52, no. 1, pp. 122–136, 2016.

[125] R. Visina, Y. Bar-Shalom, and P. Willett, "Multiple-model estimators for tracking sharply maneuvering ground targets," *IEEE Transactions on Aerospace and Electronic Systems*, vol. 54, no. 3, pp. 1404–1414, June 2018.

[126] X. Li and Y. Bar-Shalom, "Design of an interacting multiple model algorithm for air traffic control tracking," *IEEE Transactions on Control Systems Technology*, vol. 1, no. 3, pp. 186–194, 1993.

[127] Z. Kowalczuk and M. Sankowski, "Soft- and hard-decision multiple-model estimators for air traffic control," *IEEE Transactions on Aerospace and Electronic Systems*, vol. 46, no. 4, pp. 2056–2065, October 2010.

[128] S. Kim, J. Choi, and Y. Kim, "Fault detection and diagnosis of aircraft actuators using fuzzy-tuning IMM filter," *IEEE Transactions on Aerospace and Electronic Systems*, vol. 44, no. 3, pp. 940–952, July 2008.

[129] N. Sadeghzadeh-Nokhodberiz and J. Poshtan, "Distributed interacting multiple filters for fault diagnosis of navigation sensors in a robotic system," *IEEE Transactions on Systems, Man, and Cybernetics: Systems*, vol. 47, no. 7, pp. 1383–1393, July 2017.

[130] M. Mabrouk, G. Ferre, E. Grivel, and N. Deltimple, "Interacting multiple model based detector to compensate power amplifier distortions in cognitive radio," *IEEE Transactions on Communications*, vol. 63, no. 5, pp. 1580–1593, May 2015.

[131] X. Feng, Y. Zhao, Z. Zhao, and Z. Zhou, "Cognitive tracking waveform design based on multiple model interaction and measurement information fusion," *IEEE Access*, vol. 6, pp. 30 680–30 690, 2018.

[132] R. Li, X., and Y. Bar-Shalom, "A recursive multiple model approach to noise identification," *IEEE Transactions on Aerospace and Electronic Systems*, vol. 30, no. 3, pp. 671–684, July 1994.

[133] H. Blom and Y. Bar-Shalom, "The interacting multiple model algorithm for systems with Markovian switching coefficients," *IEEE Transactions on Automatic Control*, vol. 33, no. 8, pp. 780–783, August 1988.

[134] M. Kenny, "Ever wondered what is on the Orbcomm satellite downlink?" http://mdkenny.customer.netspace.net.au/Orbcomm.pdf, 2002.

[135] Z. Kassas, V. Ghadiok, and T. Humphreys, "Adaptive estimation of signals of opportunity," in *Proceedings of ION GNSS Conference*, September 2014, pp. 1679–1689.

[136] N. Khairallah and Z. Kassas, "Ephemeris closed-loop tracking of LEO satellites with pseudorange and Doppler measurements," in *Proceedings of ION GNSS Conference*, September 2021, pp. 2544–2555.